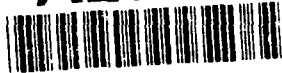


2

Fermi Level Modulation at Optical Frequencies and
Photoemission in a Metal-Barrier-Superconductor
Tunneling Element

AD-A251 273



by

Timothy J Creamer
B.S. Loyola College
(1982)

DTIC
ELECTE
MAY 28 1992
S A D

Submitted to the Department of Physics
in partial fulfillment of the requirements for the degree of
Master of Science in Physics
at the

Massachusetts Institute of Technology

May 1992

© Massachusetts Institute of Technology 1992

Signature of Author.....

Department of Physics

May 8, 1992

Certified by

Ali Javan

Professor of Physics

Thesis Supervisor

Accepted by.....

George F. Koster

Chairman, Departmental Committee on Graduate Students

This document has been approved
for public release and sale; its
distribution is unlimited.

92-13247



92 5 18 1992

**Fermi Level Modulation at Optical Frequencies and
Photoemission in a Metal-Barrier-Superconductor
Tunneling Element**

by

Timothy J Creamer

submitted to the Department of Physics
on May 8, 1992, in partial fulfillment of the
requirements for the degree of
Master of Science in Physics

Abstract

40 μ m by 40 μ m metal-barrier-superconductor electron tunneling elements' responses to visible laser light from an Argon Ion laser are examined. Through an in-depth analysis of the major current producing processes, it is shown that once the impinging E-field is coupled across the barrier, the dominant response results from the modulation of the Fermi level at the applied optical frequency, producing a rectified current due to the nonlinear characteristics of the inelastic tunneling process. The associated implications of this with respect to modulation of a superconducting tunneling current at an optical frequency are discussed, leading to applications such as absolute frequency measurements as well as a master-clock oscillator operating at an optical frequency.

Thesis Supervisor: Ali Javan

Title: Professor of Physics

Statement A per telecon
Capt Jim Creighton TAPC/OPB-D
Alexandria, VA 22332-0411

NWW 5/27/92



Accession For	
NTIS CRA&I	<input checked="" type="checkbox"/>
DTIC TAB	<input type="checkbox"/>
Unannounced	<input type="checkbox"/>
Justification	
By	
Distribution/	
Availability Codes	
Dist	Avail and/or Special
A-1	

Acknowledgments

So many individuals have played so great a part in the ultimate production of this thesis. In particular I would like to recognize the following:

First, and foremost, my utmost appreciation to Professor Ali Javan for his gentle guiding, insights, tutelage and care. Without the risk he took by permitting me to work with him, this thesis would not have been possible. It has been an honor and privilege to have worked for and with him. May all students of physics be as fortunate.

Jaagedeesh Moodera without whose help, wisdom, apparatus and guidance, the junctions would never have been made. It was his diligence and willingness to share his experience that allowed us overcome almost 9 months of difficulty with the initial elements. All the credit for the fabrication of all the junctions belongs with him and his lab!

Larry Saul whose insights and talents provided us some rapid and accurate computer solutions to the nastier of problems, and whose appreciation of physics allowed me to use him as a sounding board for some of my more inane and inappropriate ideas without embarrassment.

The soldiers of the 82d Airborne Division's Aviation Brigade and the soldiers of the 1st Armored Division's Aviation Brigade for their support and loyalty. It is due to their efforts that my career was successful enough to permit me the opportunity to study at MIT.

Dr. Michael Otteson, a man of immeasurable patience, . . . whose patience I am sure I measured on several occasions. It would be no exaggeration to say that this project is a direct and immediate result of his instruction, mentoring, diligence, experience, talent and tenacity. He set up the apparatus, ran the experiments with me, trouble-shot, corrected, and fine tuned all we did. He has educated me from an unaware and ignorant ball-and-chain to a contributing member of our research team. Not only is it fair to say, that in the short time we have worked together he has instilled an immense amount of physics knowledge and awareness in me, but he has also shown me how to think! This thesis is as much his as mine. Thanks, Mike.

My wife, who once again lovingly tolerates my single-minded determination to accomplish a goal, often at the expense of our family time. Without her, my life would be incomplete (and I would probably be hungry). As in all of my endeavors, she is the last to be thanked, mostly since there are not enough words to express my sincerest appreciation for her understanding, love, and patience.

And, finally, to Patrick -- our bundle of joy!

"On December 12, 1960, at 4:20 pm (EST), the initial ideas that make this work possible came to light."

Contents

1. Introduction	
1.1 History	6
1.2 Thesis Structure	8
2. Tunneling Theory	
2.1 1-Dimensional	10
2.2 Metal-Barrier-Metal (M-B-M)	12
2.3 Metal-Barrier-Superconductor (M-B-S)	18
2.4 Current Producing Responses	
2.4.1 Photoemission	22
2.4.2 Rectification	26
2.4.3 Temperature Effect	28
3. Experimental Arrangement	
3.1 Junctions	32
3.2 Cryogenic Apparatus and Optics	35
3.3 Barrier Height Determination	37
3.4 I-V, and I ² -V	39
4. Metal-Barrier-Superconductor Response	
4.1 Barrier Height	44
4.2 Photoemissive and Thermal Contributions	47
4.3 Fermi Level Modulation at Optical Frequencies -- Rectification Response and Conclusion	55
5. Future Work	70
6. Appendices	73

Chapter 1

1.1 Introduction

Since the outset and formulation of quantum mechanics, many of the described phenomena clash with a common sense (classical) appreciation. Of these, tunneling can be offered as the most striking. Classically, a barrier is a barrier not to be trespassed: a ball, with an insufficient amount of energy to scale the wall, will return from bouncing off the wall. The trick, of course, is to use really tiny little balls, and lots of them. Quantum mechanics maintains then, that if the wall is sufficiently thin, a fraction of those balls can tunnel through.

Tunneling followed directly from Schrödinger's equation, and was used to explain¹ several phenomena that were coming to light around the time of Schrödinger's original paper, such as: the field ionization of atomic hydrogen by Oppenheimer (1928), field emission from a free-electron metal by Fowler and Nordheim (1928), alpha decay by Gamow (1928), and metal-insulator-metal junctions by Sommerfeld and Bethe (1933).

Almost thirty years later, the tunneling phenomenon fell under the scrutiny of the engineers when in 1957 Esaki developed his tunnel diode, spurring this field of thought to a new height of interest. Shortly thereafter (1960), Giaever as well as Josephson studied metal-insulator-superconductor and superconductor-insulator-superconductor tunneling. Since this time, many experiments have been accomplished using tunneling as a means to probe the superconductor's energy gap.

¹For an exhaustive history and references, see Solymar, pp. 3, 19, 29-31, 54-55.

More recently, however, as a result of the research breakthroughs at the MIT Optical and Infrared Laser Laboratory, attentions have turned toward high-speed tunneling junctions with applications as optical frequency mixers [2][4-5][48-49]. These metal-oxide-metal point contact junctions form a class of high-speed elements with the novel capabilities of responding to an applied optical field at the applied optical frequency. As a result of this work, it was possible to mix microwave and far infrared radiation, taking advantage of the slight nonlinearities of the elastic tunneling (current flowed through the contact region as a nonlinear function of the electric potential applied across it). The first optical frequency mixing experiments were performed using a high speed adaptation of a microwave rectifying, metal-semiconductor (forming a Schottky barrier), point contact diode[4], successfully generating harmonics of microwave radiation mixing with $337 \mu\text{m}$ ($\sim 10^{12}$ Hz) radiation. This could occur because the capacitor-like junction could oscillate at these frequencies.

However, the intrinsic time-constant limitations of the semiconductor element necessitated a different approach for higher speed work. This resulted in polished metal posts replacing the semiconductor [5], forming a metal-barrier-metal junction, which were then responsible for frequency mixing out to $1.5 \mu\text{m}$ [48]. But the associated inherent vibration sensitivity of this geometry precluded its further study in the search for faster responses.

In order to better understand and to study the physical processes of electron tunneling of the metal-barrier-metal junctions lead to the geometry of the thin-film metal-crosses that were used by Elchinger [1] and were used in this work, and whose dimensions were on the order of tens of microns. These crosses are, in effect, a tiny capacitor formed by evaporating a thin,

metal strip onto a quartz substrate, oxidizing it, and then sandwiching this oxide layer with the second metal strip. Judiciously choosing one of these metals such that it goes superconducting at a convenient cryogenic temperature, it is then possible to take advantage of the inherent and much more significant, tunneling nonlinearities due to the band-gap effect of the metal-oxide-superconductor electron tunneling element.

Until the present work, several investigators have studied the response of these same type junctions to electric fields whose frequencies were at about the $(RC)^{-1}$ time constant of the junction as well as at higher frequencies [6-10]. They concluded that the lower frequency (in the Rf) response mechanism arose from the nonlinearities of the junction's I-V characteristics and was due to rectification as a result of the modulation of the Fermi level across the barrier, but that the higher frequency (in the far and near IR) response was due to a photo induced tunneling [1].

As a result of this work, it can be shown that the junction's response to the higher frequency (up to the IR and visible), contrary to the earlier works, is indeed due to modulation of the Fermi level across the barrier at the applied frequency, causing rectification, and that this process can be made to dominate over others. This is important in that it is possible to take advantage of the higher order of nonlinearity (those far exceeding that of a normal metal-barrier-normal metal junction) in order to accomplish frequency mixing well into the visible and even into the UV.

1.2 Thesis organization

The purpose of this thesis is to examine the response of a metal-barrier-superconductor when it is exposed to light. Several processes are involved, some of which are competing, while some have nearly the same response

shape. The matter at hand, then, is to show under what conditions each process dominates.

There are several steps in making this identification, and as such, lend themselves nicely to the thesis organization:

- Chapter 2 outlines the basic theory of tunneling, to include the 1-dimensional basics, metal-insulator-metal tunneling, and metal-barrier-superconductor tunneling. In addition, the processes of photoemission, rectification resulting from Fermi level modulation across the barrier, and how a differential temperature change (due to the junction being heated) can manifest itself in an observed signal are all discussed.

- Chapter 3 describes the experimental setup and the procedures used to collect the data.

- Chapter 4 details the data analysis in determining the associated barrier parameters, compares theoretical predictions with experimental results for the I-V curves as well as the associated derivative curves, and accommodates earlier interpretations.

- Chapter 5 deals primarily with the implications of this work, improvements, and future experiments that can and will dovetail from these findings to include more efficient ways to couple the light across the junction, how to make higher speed junctions, and the future of frequency mixing and absolute frequency measurements.

- Finally, several appendices have been included for ready reference and clarity. The first appendix details from a microscopic view the constancy of the superconductive calculations with the corrective factor of a change in density of states; the second appendix outlines the advantage of four-pole impedance measurements, and the third appendix describes the Cray X-MP FORTRAN subroutine used to numerically evaluate the I-V integrals.

Chapter 2

Tunneling Theory

2.1 One-Dimensional²

Much insight and relevance can be gleaned about the processes of interest in this experiment by starting from basic principles, and examining even the one-dimensional case.

An electron moving with a kinetic energy of E in zero potential is incident upon a potential barrier U_2 , such that $U_2 > E$, as shown in Figure 1.

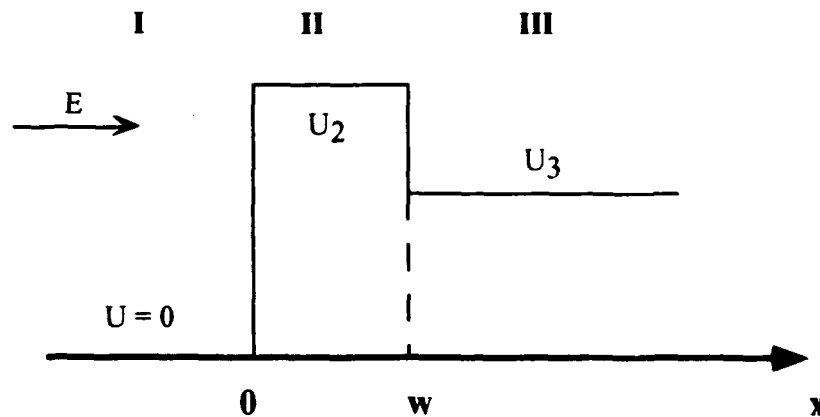


Figure 1 -- One-dimensional potential barrier.

Now, from the time-independent Schrödinger equation, we can work out the probability of the electron appearing on the other side of the barrier

$$\left(-\frac{\hbar}{2m}\nabla^2 + U\right)\psi = E\psi \quad (2.1.1)$$

²theory for this chapter has been taken from the following references: [11], [12], [3, pp 20-21].

For a constant potential in region I, we can find the wave equation of the electron to be

$$\psi_1 = A \exp(i k_1 x) + B \exp(-i k_1 x) \quad (2.1.2)$$

where

$$k_1 = \frac{(2mE)^{1/2}}{\hbar} \quad (2.1.3)$$

Now the solutions in regions II and III are

$$\psi_2 = C \exp(-k_2 x) + D \exp(k_2 x) \quad (2.1.4)$$

$$\psi_3 = F \exp(i k_3 x) \quad (2.1.5)$$

where

$$k_2 = \frac{1}{\hbar} [2m(U_2 - E)]^{1/2} \quad \text{and} \quad k_3 = \frac{1}{\hbar} [2m(U_3 - E)]^{1/2} \quad (2.1.6)$$

and A, B, C, D, F are constants which we can determine by imposing the condition that the wave function is smooth and continuous. Hence, at the boundaries $x = x_1$, and $x = x_2$, ψ and $d\psi/dx$ must be continuous. Now the quantity of real interest is $|F/A|$, the amplitude relationship between the output and the input. Assuming that $k_2 w \gg 1$, then $\exp(-k_2 w)$ is negligible compared to $\exp(k_2 w)$, and it is possible to show that

$$\left| \frac{F}{A} \right| = \frac{4k_1 k_2}{(k_1^2 + k_2^2)^{1/2} (k_3^2 + k_2^2)^{1/2}} \exp(-k_2 w) \quad (2.1.7)$$

Now, we can obtain the ratio of current densities, such that

$$\frac{j_3}{j_1} = \frac{k_3}{k_1} \left| \frac{F}{A} \right|^2 = \frac{16k_1 k_3 k_2^2}{(k_1^2 + k_2^2)(k_3^2 + k_2^2)} \exp(-2k_2 w) \quad (2.1.8)$$

What is of extreme importance here is that the above expression is dominated by the exponential factor. Consequently, the wider the barrier is, the smaller the current that can flow across it. From many previous studies, practical barriers in solids tend to be on the order of 1 eV. Using this value for $(U_2 - E)$ in Equation (2.1.6), taking the free electron mass, and a current transmission of 10^{-6} , then the width of the barrier should be on the order of

$$w = \frac{1}{2k_2} \ln 10^6 \approx 10^{-9} \text{ m} \quad (2.1.9)$$

in order to observe tunneling.

2.2 Metal-Barrier-Metal (MBM) Tunneling³

Before discussing metal-barrier-superconductor tunneling, it would be best to lay the groundwork with first a short investigation of metal-barrier-metal tunneling. From a simple model (Figure 2a), it is possible to see that in thermal equilibrium the Fermi levels of the two metals are equal. Now, defining a net positive electron flow as being from left to right, when a negative voltage is applied to the metal on the left, all the electrons of that metal will have, then, an energy eV higher. As a result, the relative Fermi energies can be depicted as in Figure 2b.

³theory for this chapter has been taken from the following references: [13],[14]. [15,pp 31-46], [3, pp. 22-23].

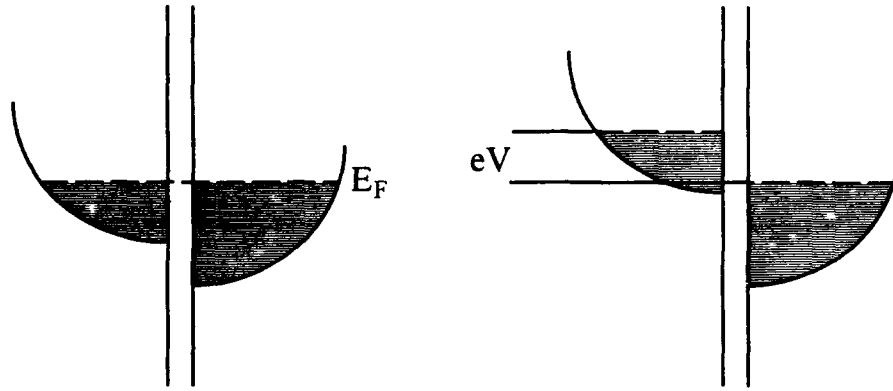


Figure 2 -- Fermi energy diagram for a metal-barrier-metal junction.(a) Thermal equilibrium; (b) at a potential difference of V.

There are several approaches to calculate the current flowing across the junction, but here it will be sufficient to say that the number of electrons moving from left to right in an energy interval dE must be proportional to the number of occupied states on the left. In other words,

$$N_l(E - eV) f(E - eV) dE \quad (2.2.1)$$

where N_l is the density of states of the metal on the left, and f is the Fermi function (taking the reference point as being the Fermi level of the metal on the right, since in the experiment, it is the grounded metal). Now, for there to be a current moving from left to right there must be unoccupied states in the metal on the right. In other words, the current must also be proportional to

$$N_r(E) [1 - f(E - eV)] dE \quad (2.2.2)$$

where N_r is the density of states of the metal on the right. Incorporating all the above with the probability of transition across the barrier, $P_{l \rightarrow r}(E)$, the current flowing from left to right is

$$I_{l \rightarrow r} \sim P_{l \rightarrow r}(E) N_l(E - eV) f(E - eV) N_r(E) [1 - f(E - eV)] dE \quad (2.2.3)$$

while the current flowing from right to left is

$$I_{r \rightarrow l} \sim P_{r \rightarrow l}(E) N_l(E - eV) f(E - eV) N_r(E) [1 - f(E - eV)] dE \quad (2.2.4)$$

Making the assumption that $P_{l \rightarrow r}(E) = P_{r \rightarrow l}(E)$, (that is, an electron has just as much chance to tunnel from left to right as from right to left), and integrating over all energies, the net current becomes

$$I \sim \int P_{l \rightarrow r}(E) N_l(E - eV) N_r(E) [f(E - eV) - f(E)] dE \quad (2.2.5)$$

Now, interestingly, for small applied voltages, it is not uncommon to take $P_{l \rightarrow r}(E)$ as being independent of energy, thus removing it from under the integral. Similarly, it can be argued that the density of states is a slowly varying function, and simply take its value at the Fermi level, or

$$N_l(E - eV) \approx N_l(E) = N_l(0) \quad \text{and} \quad N_r(E) \approx N_r(0) \quad (2.2.6)$$

Incorporating the geometry considerations of the barrier/junction as well as the $P_{l \rightarrow r}(E)$ into A , the expression for the current reduces to

$$I = A N_l(0) N_r(0) \int [f(E - eV) - f(E)] dE \quad (2.2.7)$$

This then allows the Fermi functions to be expanded for small voltages to yield

$$[f(E - eV) - f(E)] = -eV \frac{df}{dE} \quad (2.2.8)$$

which, if the temperature is not too high, $-\frac{df}{dE}$ can be approximated by a delta function, giving

$$I = A N_l(0) N_r(0) eV \quad (2.2.9)$$

In short then, a metal-barrier-metal junction obeys Ohm's Law, with a linear relationship between current and voltage.

The above heuristic approach was convenient, but to validate its simplicity a basic set of states, a perturbing Hamiltonian, a final set of states, and a matrix element connecting the two states should be analyzed. This approach was actually tackled by Bardeen [16] first, then later by Kane [15, pp. 1-12] in greater detail.

ψ_2 in Equation (2.1.4) represents an exact solution of Schrödinger's equation in region II, where there are two exponential functions decreasing in the positive and negative directions. Rewriting these two functions

$$\psi_l = C_l \exp(-k_2 x) \quad \text{and} \quad \psi_r = C_r \exp(-k_2 x) \quad (2.2.10)$$

Now, assume that ψ_l is a solution not only for $x_1 < x < x_2$, but for the whole region $x > x_1$. This incurs only a slight error since ψ_l is already extremely small at $x = x_2$. Similarly, consider ψ_r as a solution for $x < x_2$. Assuming,

then, that an electron is in the initial state of ψ_i , it is possible to work out its transition rate into ψ_r . For the complete time-dependent wave function

$$\Psi = q(t) \psi_i \exp\left(-i \frac{E_i}{\hbar} t\right) + r(t) \psi_r \exp\left(-i \frac{E_r}{\hbar} t\right) \quad (2.2.11)$$

Substituting the above equation into the time-dependent Schrödinger equation

$$H\Psi = i\hbar \frac{\partial \Psi}{\partial t} \quad (2.2.12)$$

and assuming that only a very small proportion of electrons make the transition (thus, implying $q \approx 1$, and $r \approx 0$), and that the electrons are either in ψ_i or ψ_r , it follows that $dq/dt \approx 0$. Using this, multiplying both sides of the equation by ψ_r^* and integrating yields

$$i\hbar \frac{dr}{dt} = \int \psi_r^* (H - E_i) \psi_i dx \exp\left(i \frac{E_r - E_i}{\hbar} t\right) \quad (2.2.13)$$

Writing the Hamiltonian H in the form of $H_0 + H_1$ and noting that $H_0 \psi_i = E_i \psi_i$ yields

$$\int \psi_r^* (H - E_i) \psi_i dx = \int \psi_r^* H_1 \psi_i dx \quad (2.2.14)$$

so that now the effective tunneling matrix element may be defined by

$$T_{r,i} = \int \psi_r^* (H - E_i) \psi_i dx \quad (2.2.15)$$

Now, in review, the essential assumptions in the above derivation were that ψ_l and ψ_r were good approximate solutions of the exact Hamiltonian H , and exact solutions of the hypothetical 'unperturbed' Hamiltonian H_0 , and thus $H\psi_l = E\psi_l$ for $x < x_2$, and $H\psi_r = E\psi_r$ for $x > x_1$. Hence the integral

$$-\int_{x_B}^{\infty} \psi_l(H - E_r)\psi_r^* dx \quad x_B \geq x_1 \quad (2.2.16)$$

is zero, and may be added to the integral in Equation (2.2.15) yielding the symmetric form

$$T_{rl} = \int_{x_B}^{\infty} [\psi_r^*(H - E_l)\psi_l - \psi_l(H - E_r)\psi_r^*] dx \quad x_1 \leq x_B \leq x_2 \quad (2.2.17)$$

Integrating by parts yields

$$T_{rl} = -\frac{\hbar}{2m} \left(\psi_r^* \frac{d\psi_l}{dx} - \psi_l \frac{d\psi_r^*}{dx} \right)_{x_B} \quad (2.2.18)$$

which, upon substituting Equations (2.2.10) into the above gives

$$T_{rl} = \frac{\hbar^2 k_2}{m} C_r^* C_l \quad (2.2.19)$$

With this matrix element, the current may be determined by using Fermi's Golden Rule, yielding the same expression that was obtained for the transmitted current before. This is critical, for it shows that the Bardeen approach provides the same result as the simple one-electron calculation.

2.3 Metal-Barrier-Superconductor⁴

Using the usual semi-conductor representation, Figure 3 shows a junction formed by sandwiching a thin insulating barrier between a normal metal and a superconductor. At absolute zero temperature, all of the states in the superconductor are filled up to $E_F - \Delta$, with no filled states above the gap.

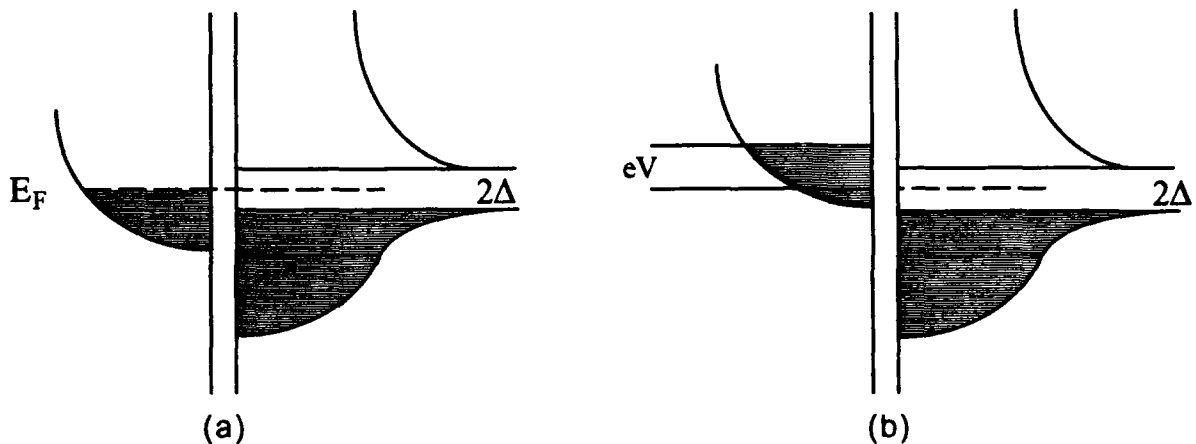


Figure 3 -- Energy diagram of a metal-barrier-superconductor junction at $T = 0^\circ\text{K}$, (a) $V = 0$; (b) $V > \Delta/e$

When in thermal equilibrium, the Fermi energies must match (Figure 3a). When a voltage $V < \Delta/e$ is applied, the electrons on the left have no empty states on the right to access, and thus no current flows. At $V = \Delta/e$, there is a sudden increase in current, not only because now electrons may tunnel from left to right, but they also face a large density of available states. As the voltage is increased further, even more empty states become available for tunneling and the current increases as indicated in Figure 4.⁵

⁴theory for this chapter has been taken from the following references: [3, pp.32-39], [17], [18].

⁵For an extremely palatable account of the first works in this area, see [17].

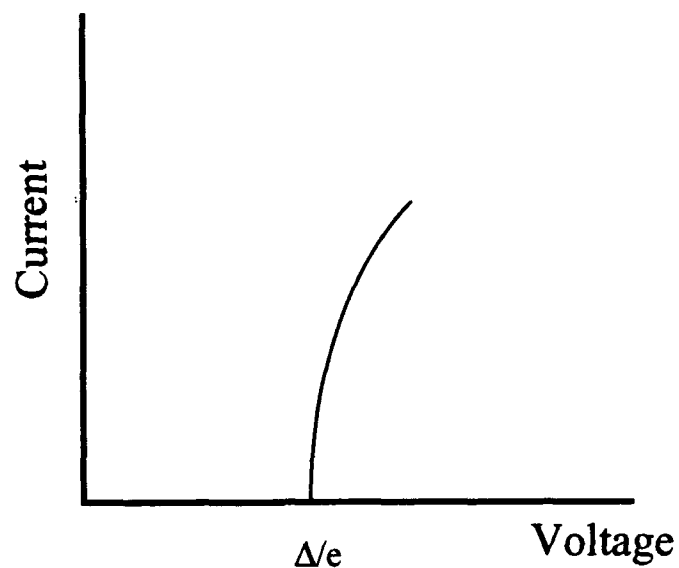


Figure 4 -- The I-V response from a metal-barrier-superconductor at $T=0^{\circ}\text{K}$

Now, at finite temperatures (Figure 5), there are electrons above $E_F + \Delta$, as well as holes below this gap. In addition, some of the electrons of the normal metal are in excess of $E_F + \Delta$, even at thermal equilibrium.

Consequently, even a tiny voltage is sufficient to initiate a current, but a sizable rise in current will again occur at $V = \Delta/e$ (Figure 6)

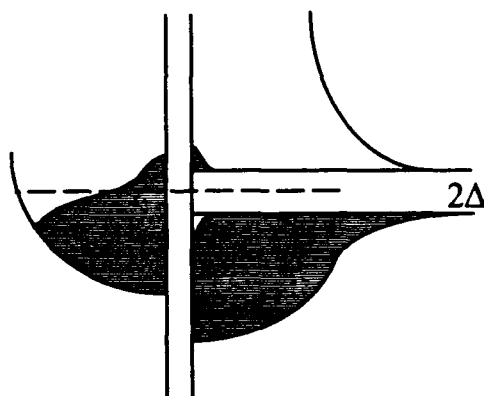


Figure 5 -- Energy diagram for a metal-barrier-superconductor at $T > 0^{\circ}\text{K}$, in thermal equilibrium

I-V Curve from an Al-Al Oxide-VTi (M-B-S) Junction
($T=1.7^{\circ}\text{K}$)

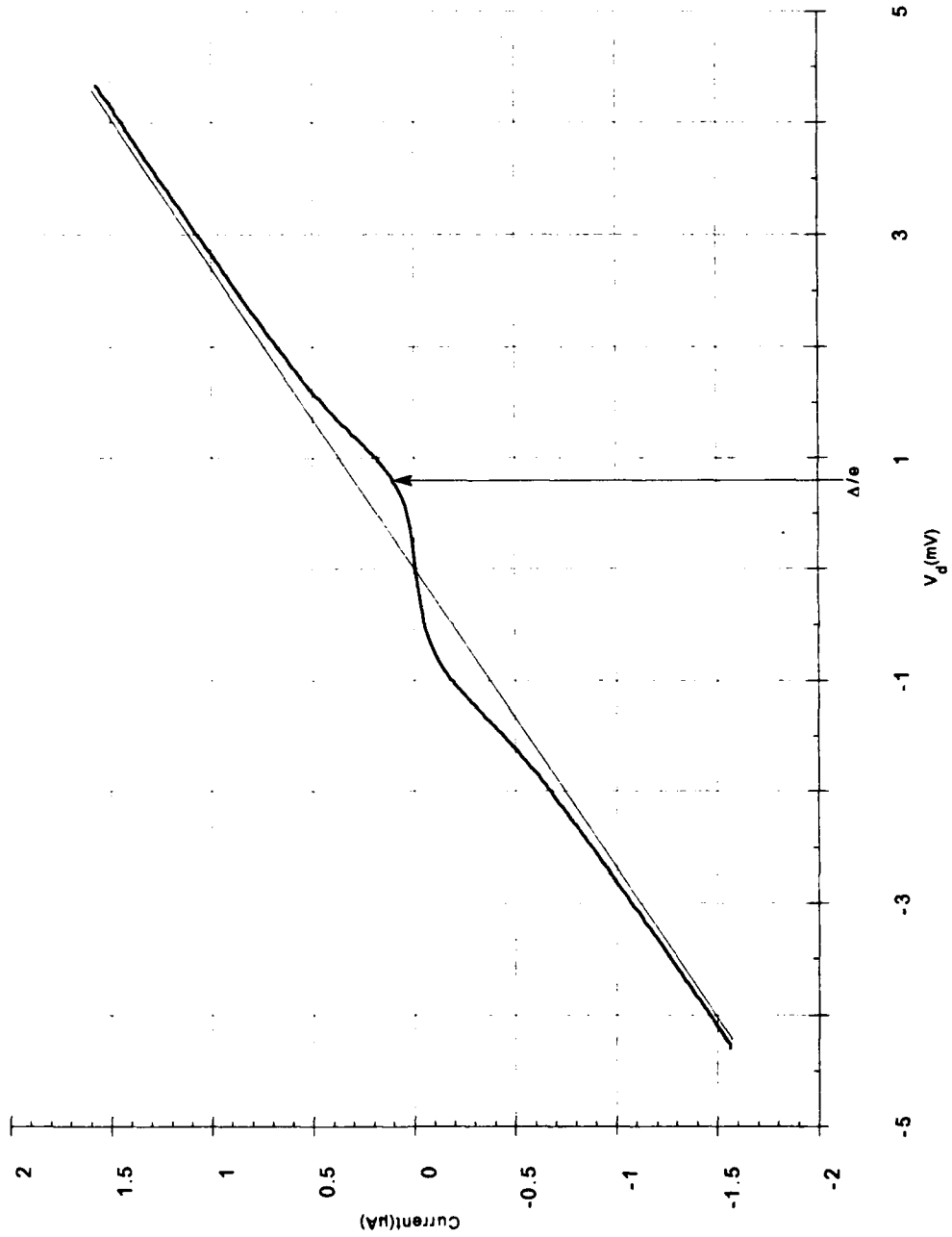


Figure 6 -- Current vs Bias Voltage, Illustrating the Nonlinear Response Due to the Band Gap of the Superconductor (Straight line depicts Ohmic response when VTi is nonsuperconducting)

With this background, and the formalism of section 2.2, it is possible to develop an expression for the current that will flow through a metal-barrier-superconductor junction. The essential assumption is that when the metal goes superconducting, only the density of states changes, but nothing else does (the matrix element remains the same)⁶. Consequently, Equation (2.2.7) may be used to describe this current, provided the density of states of the superconductor is taken into account. That is, replacing $N_r(E)$ by the density of states in the superconductor, N_s ,

$$N_s(E) = N_N(E) n_s(E) \quad (2.3.1)$$

where N_N is the density of states of that metal in the normal state, and n_s is the BCS superconductor, energy gap-dependent, density of states correction term. Now the current may be written as

$$I_{NS} = A N_{lN}(0) N_{rN}(0) \int n_s(E) [f(E-eV) - f(E)] dE \quad (2.3.2)$$

where N_{lN} and N_{rN} refer to the normal metal density of states of the metals on the left and right, respectively, in Figure 5. At $T = 0$, the Fermi function is unity up to $f(0)$, and takes the value zero above that. This then modifies the above expression for the current to

⁶See appendix 1.

$$I_{NS} = A N_{IN}(0) N_{rN}(0) \int_{\Delta}^{eV} \frac{E dE}{(E^2 - \Delta^2)^{1/2}} \quad (2.3.3)$$

$$= A N_{IN}(0) N_{rN}(0) [(eV)^2 - \Delta^2]^{1/2} \quad (2.3.4)$$

for $eV > \Delta$, while $I_{NS} = 0$ for $eV < \Delta$.

Now, when $T > 0$, it is necessary to integrate over all possible energies so that

$$I_{NS} = A N_{IN}(0) N_{rN}(0) \int \frac{|E| [f(E-eV) - f(E)] dE}{(E^2 - \Delta^2)^{1/2}} \quad (2.3.5)$$

Although this has been solved in closed form for $eV < \Delta$ (with some simplifying assumptions) by Giaever and Megerle [19], the predominant region of this present work's interest lies just prior to where the junction's response goes Ohmic. As a result, numerical integrations⁷ were required to calculate the predicted curves for the metal-barrier-superconductor junctions that were used.

2.4 Current Producing Responses⁸

2.4.1 Photoemission

Now that the ground work for the experimental conditions of the tunneling element has been set, this leads to the discussions involving the mechanisms that yield current producing responses. From the vast amount of

⁷see appendix #3.

⁸theory for this section has been taken from the following references: [1], [14], [29].

work that has already been done in this area [20-28], the dominant current producing junction responses are due to photoemission, rectification, and a thermally induced current.

Photoemission and its bevy of intricacies have been studied extensively. Applying the formulations to this tunneling junction environment, Stratton [14], Burshtein and Levinson [29], Elchinger [1], and Jaklevic and Lambe [30] have already compiled the detailed derivations. Following predominantly Stratton's approach, the equation describing the photoemissive current for a trapezoidal barrier (Figure 7) can be obtained.

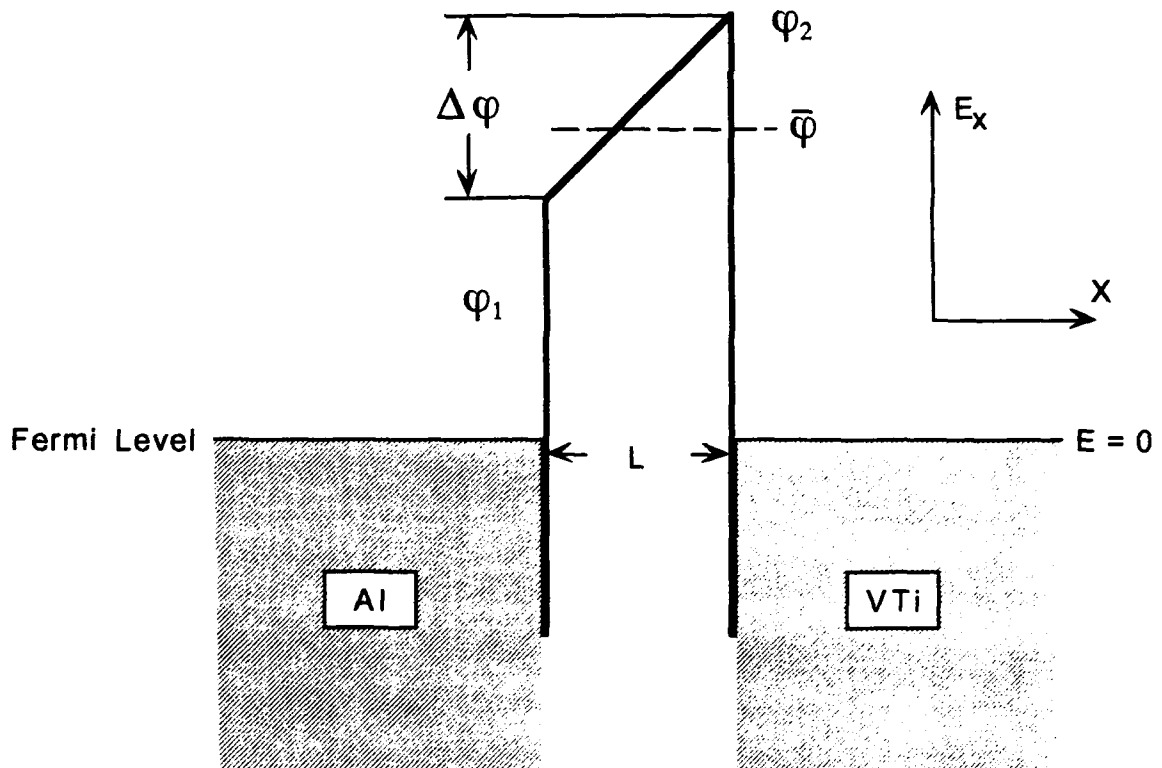


Figure 7 -- Trapezoidal Barrier

Amending the one-dimensional approach to contain electrons moving in all three axial directions, the current density can once again be written phenomenologically as the product of the flux of normally incident electrons on the barrier at energy E_x potentially contributing to the current, and the probability of penetration through the barrier, integrated over all applicable E_x .

$$J = \int_{-eV_b}^{E_{\max}} F(E_x, V_b) P(E_x, V_b) dE_x \quad (2.4.1)$$

Simmons computes the electron current density per unit energy (the supply function) by averaging the electron energy density parallel to the barrier (i.e., in the y and z directions), leaving only the x-directed flux. Consequently,

$$F(E_x) = \frac{4\pi m e}{h^3} \int_0^{\infty} f(E_x, E_r) dE_r \quad (2.4.2)$$

where

$$f(E_x, E_r) = \frac{1}{1 + e^{\beta E_r} e^{\beta E_x}} \quad (2.4.3)$$

Now, integrating over all radial energy, E_r ,

$$F(E_x) = \frac{4\pi m e (kT)}{h^3} \ln(1 + e^{-\beta E_x}) \quad (2.4.4)$$

where e is the electronic charge, h is Planck's constant, k is Boltzmann's constant, T the temperature of the electrode, and β is merely $1/kT$. Just as before, the net current will simply be determined by the difference in supply functions induced by an external bias voltage, V_b , such that

$$J_{\text{Tot}} = J_{l \rightarrow r} - J_{r \rightarrow l} = \frac{4\pi m e (kT)}{h^3} \int_{-eV}^{\infty} P(E_x) \ln \left[\frac{1 + e^{-\beta E_x}}{1 + e^{-\beta(E_x - eV)}} \right] dE_x \quad (2.4.5)$$

Now, unlike the rectification response where the Fermi level at the barrier oscillates at the applied electric field frequency, the photoemissive current is a DC effect, where only a fraction of the electrons in the Fermi sea contribute. Assuming that the absorbed light will be equally partitioned among the three orthogonal velocity components, and that initially the light illuminates only the normal metal side (the left side in Figure 7), then, at $V_b = 0$ only electrons with an energy $-h\nu$ will contribute to the current. This results in having to shift the supply function from E_x to $(E_x - h\nu)$ in order to account for these electrons. Of all the electrons that are photoexcited, only a fraction, f , of them will have their velocities directed in the x-direction. As a result then, the photocurrent can be written as

$$J_{P.E.l \rightarrow r} = \frac{4\pi m e (kT)}{h^3} f \int_0^{\infty} P(E_x) \ln[1 + e^{-\beta(E_x - h\nu)}] dE_x \quad (2.4.6)$$

During this experiment $\beta = 1 / [(0.086 \text{ meV}/^\circ\text{K})(2^\circ\text{K})] \gg 1 \text{ eV}^{-1}$ while the photon energies were 2.7 eV or less, allowing the approximation

$$F(E_x) = \begin{cases} 0, & \text{for } E_x \geq h\nu \\ -\frac{4\pi m e}{h^3} (E_x - h\nu), & \text{for } E_x < h\nu \end{cases} \quad (2.4.7)$$

As will be shown, $h\nu$ is above the barrier height in all frequencies, and assuming that attenuation by scattering or through other energy loss schemes is negligible, it then becomes possible to assume $P(E_x) \approx 1$.

Allowing for the superconducting side to contribute a fraction, g , of the electrons to the net current, the total photocurrent becomes

$$J_{P.E.} \cong -2 \xi (f-g) \int_{\varphi_2}^{hv} (E_x - hv) dE_x \quad (2.4.8)$$

$$\cong \xi (f-g) (hv - \varphi_2)^2 \quad (2.4.9)$$

where, $\xi = \frac{2\pi me}{h^3}$.

It is from this last expression, that the barrier height, φ_2 , is determined from a Fowler plot [31] by plotting $\sqrt{J_{P.E.}}$ versus hv , (see Figure 17), where φ_2 is the x-axis intercept

2.4.2 Rectification

Now, another conduction process characterizing the fundamental response of the metal-barrier-metal junction to electromagnetic fields is rectification, where the junction's small capacitor-like behavior oscillates at the applied frequency [1], [32]. When light is coupled across the barrier causing Fermi-level modulation at this optical frequency, the second-order nonlinearities of the I-V curve result in a rectification of the applied optical voltage, causing a DC voltage to develop across the barrier. Since this second-order effect is proportional to the second-order derivative of the I-V curve, the rectified voltage observed versus a bias voltage will trace the second derivative of the I-V curve. These second derivative features appear as resonant curves with zero's at the inflection points of the I-V curve due to the band gap dictated by the Fermi-Dirac distribution at the operating temperature. In other words, consider impressing a sinusoidal voltage

$$V(t) = v_0 \sin(\omega_0 t) \quad (2.4.10)$$

upon the DC bias voltage being applied to the junction. Assuming that the modulating potential, v_o , is small enough to produce negligible changes in $I(V_b)$, the current can be expressed as the expansion

$$I(V) = I(V_b) + \left[\frac{dI}{dV_b} \right]_{V_b} V(t) + \frac{1}{2} \left[\frac{d^2I}{dV^2} \right]_{V_b} V^2(t) + \dots \quad (2.4.11)$$

From this expression it is obvious that if the detecting apparatus averages the AC tunneling current, then only the even-powered derivatives will manifest a response since $\langle V^{(2n+1)}(t) \rangle_t = 0$, while $\langle V^{(2n)}(t) \rangle_t = (1/2)v_o^{2n}$. As a direct consequence of this, the rectified signal will appear in the second derivative term, if rectification occurs, yielding

$$I_{\text{Rect}}(V) = \frac{1}{4} \left[\frac{d^2I}{dV^2} \right]_{V_b} v_o^2 \quad (2.4.12)$$

Therefore, the second derivative of the junction's I-V curve can be plotted versus V_b , by identifying this DC rectified response.

Now, assuming a barrier shape not of a simple square barrier, but one that embodies an asymmetry such as that in Figure 7, it is possible to determine $\bar{\Phi}$, and L . Several references [14][33] describe the calculations and derivation leading to the final result of

$$R_d = \left[\frac{h^3}{8\pi m_e e} \right] \frac{\text{Sexp}[S]}{\bar{\Phi} a} = \frac{\text{Sexp}[S]}{324 \bar{\Phi} a} \quad (2.4.13)$$

where $S = 1.025 L \sqrt{\bar{\phi}}$, a is the junction area in $(\mu\text{m})^2$, R_d -- the junction's impedance -- is in Ohms, L (the barrier thickness) is in Angstroms and $\bar{\phi}$ (the average barrier height) is in units of eV (see Figure 7). From this equation, and impedance and capacitance measurements (assuming a parallel plate capacitor) of the junction, it is then possible to find ϕ_1 , L , and an asymmetry factor, α , where

$$\alpha = \frac{\Delta\phi}{2\bar{\phi}} = \frac{\phi_2 - \phi_1}{2\bar{\phi}} \quad (2.4.14)$$

once ϕ_2 has been determined from Fowler plots. Finally, it is extremely important to remember that the above results apply only when the impressed AC signal modulates the Fermi level of one electrode -- i.e., the AC field is coupled across the barrier.

2.4.3 Differential Heating

Finally, of all the current producing responses the remaining major contributing one comes about as a result of the way the experiment was conducted. As can be seen in Figures 8 and 9, by using a phase sensitive detection technique (thus requiring that the impinging laser light on the junctions be chopped) resulted in a slight distortion of the I-V curves due to thermal heating.

Since the phase sensitive detection technique determines a signal's presence by beating a reference signal against the incoming signals to be analyzed, thus differentiating the intended information from amidst the noise, it is possible to visualize an induced differential heating signal sneaking its way through into our data. The unfortunate part about this

signal, at first inspection, is that it could possibly have a very similar current response as the sought after rectified signal.

In essence, then, what the lock-in would be seeing and manipulating is

$$I(V, T + \Delta T) - I(V, T) \quad (2.4.15)$$

which is merely

$$\frac{\partial I(V, T)}{\partial T} \Delta T \quad (2.4.16)$$

That is, that the first derivative of the I-V curve with respect to temperature could possibly contribute to the rectified signal. Fortunately, as will be shown later, once the temperature dependence of the superconducting band gap is taken into account, there is no question that the observed signal is a result of rectification.

Differential Heating
Comparison of I-V Curves

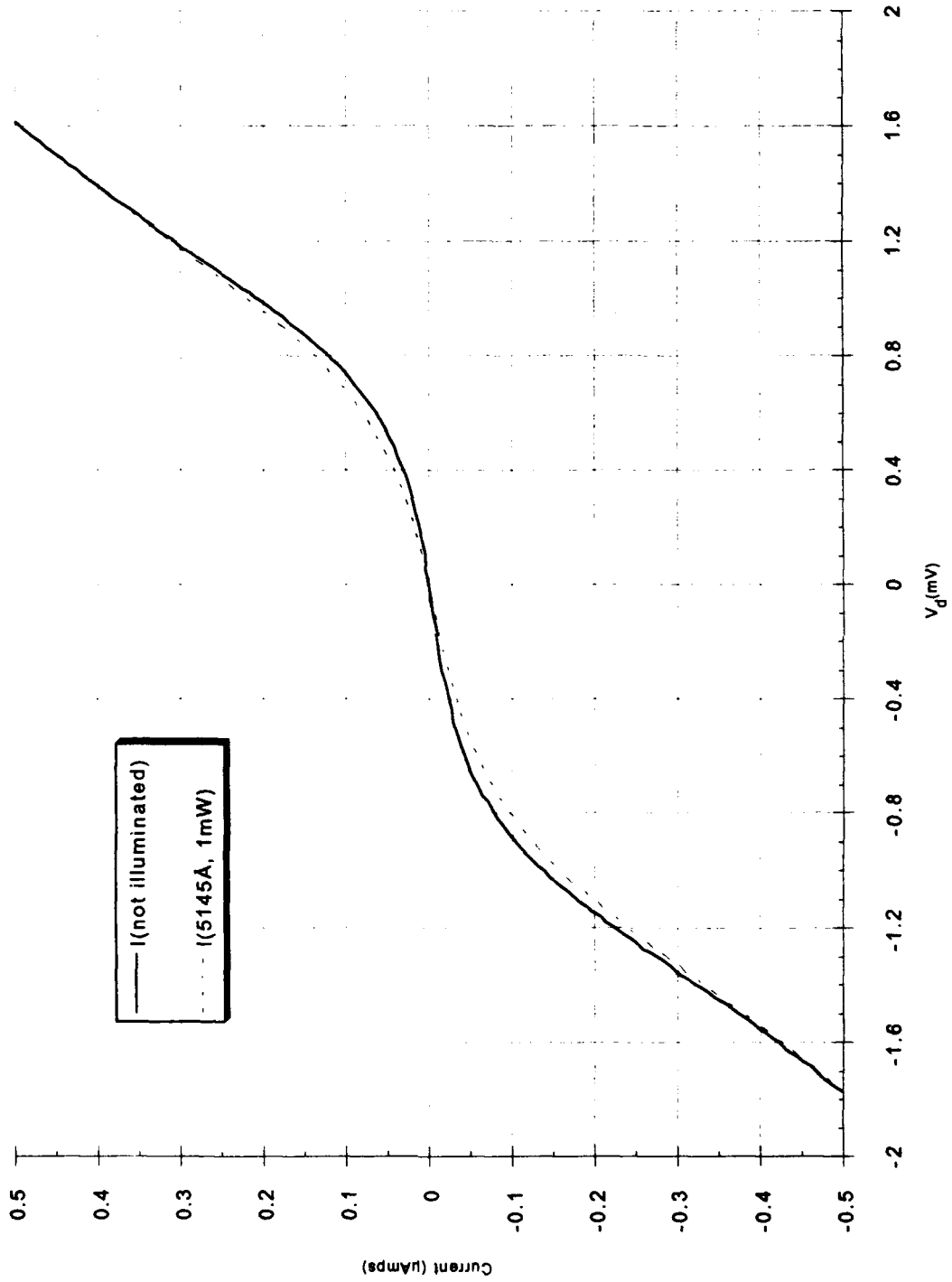


Figure 8 -- Illustration of the Heating Effect on the Junction
Due to Illumination

Calculated Differential Heating Signal
(T = 1.7°K)

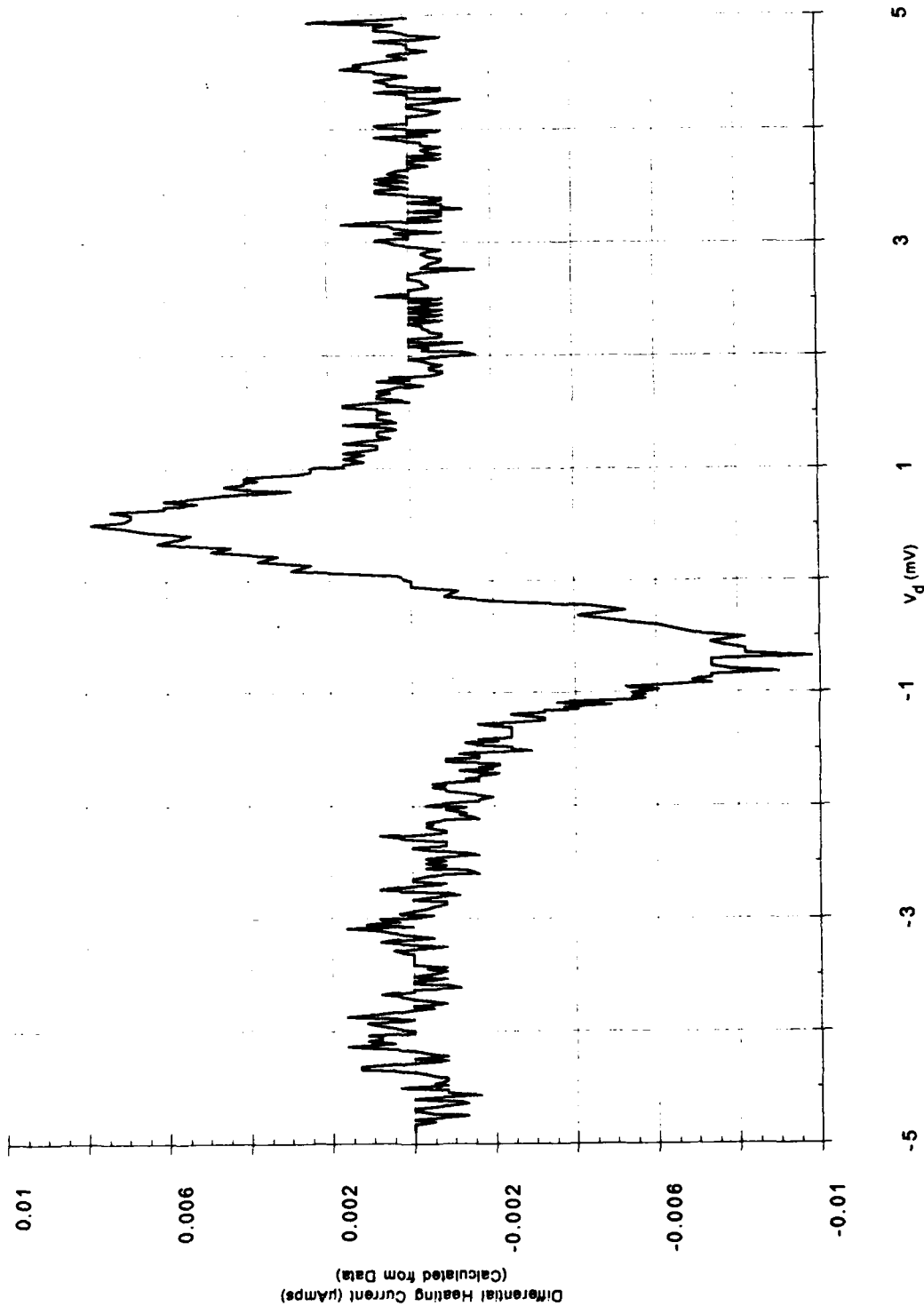


Figure 9 -- Calculated Differential Heating:
[I(V)]_{illuminated} - [I(V)]_{unilluminated}
(1mW, 5145Å)

Chapter 3

Experimental Arrangement

3.1 Junction Fabrication⁹

Crucial to the entire project was the quality and fabrication of the metal-oxide-metal/superconductor tunneling elements. These junctions were made via a metal evaporation process. Basically, the quartz substrate was masked by a thin metal plate with two identical slits in it, diagonally offset (see Figure 10). The general dimensions of these slits were 40 μ m wide by 2.75mm long. It was important to ensure that these masks were in intimate contact with the substrate, so as to avoid "bleeding" of the evaporated metal underneath the mask.

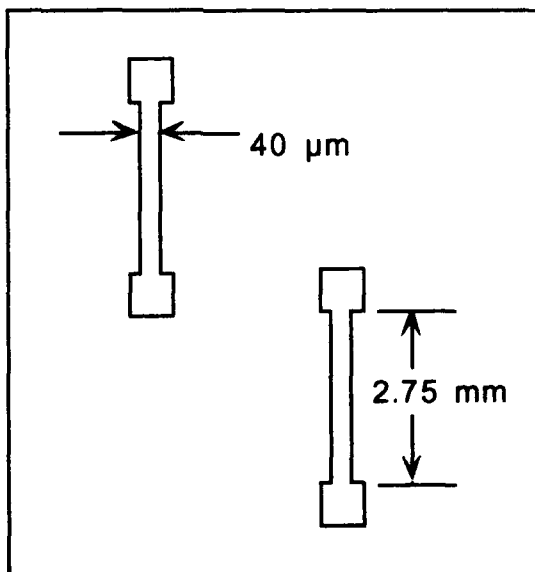


Figure 10 -- Substrate Masks for Thin Film Deposition

⁹For an in-depth discussion of the formation of metal-oxides films, see [34], [35].

Once the masks were in place, the junctions were formed by first evaporating Al to a height of 100-150Å, measured via a quartz resonator. (In addition, during the earlier attempts to refine the technique of depositing these thin films, several Sloan Dektak II stylus measurements were made to confirm lead heights). This lead was then oxidized using a glow discharge of 15-20 seconds with the overall conditions centering around 50 μ of O₂, while the discharge current was 320 mA. This typically produced an oxide thickness of about 10-20Å. Without exposing the freshly oxidized surface to the atmosphere, the masks were rotated, and the Vanadium-Titanium alloy (50%-50%) was then deposited (again by evaporation) at right angles to the two Al strips, to a height of 500Å (Figure 11). Once the VTi strip had been deposited, a new mask with a square hole was then placed on top of the junction, allowing a protective coating of 500Å of MgO to be deposited. This protected the critical area of the junction from further oxidation, moisture, and physical erosion. This completed the basic structure of the tunneling elements.

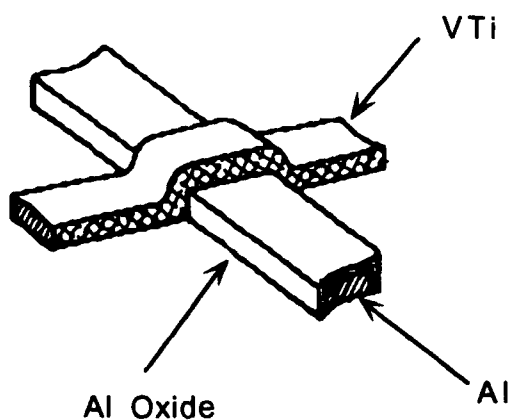


Figure 11 -- The Resulting Al-Al oxide-VTi Tunneling Element

As for the "care and feeding" of the junctions, any long term preservation was accomplished by keeping them in a desiccator, pumped down as far as the rough pumps would take it, which was approximately 30-40 μ . If these elements were exposed for too long a time to high humidity or atmosphere, there was a tendency for them to increase in impedance, sometimes reversible by vacuum pumping the samples.

For historical reasons, if for no other, it should be mentioned that for a significant amount of time, we attempted to use Al-Al oxide-Pb as the junction materials. In addition, the initial attempts were with 3 μ m wide leads. At these dimensions, and with the intended film thicknesses, it appears as if Pb's amorphous behavior was the cause of the many difficulties experienced. Not only does lead tend to migrate, but at these dimensions, dendrite formations tended to "puncture" the oxide layer, resulting in very rapid deterioration of the junction impedances. Junction lifetimes were between one and three days at room temperature, and often the thermal contraction that resulted by cooling to liquid Helium temperatures accelerated this "puncturing" deterioration. As a result, we sought a more stable superconducting metal, and found VTi. Possible adaptive solutions are noted in Chapter 5.

In order to electrically connect the junctions to the diagnostics, 36 gauge copper magnet wire was silver painted to the large square pads at the ends of the metal leads. The other ends of these magnet wires were then hard soldered into a printed circuit card that had a hole cut in the middle of it (to allow the laser light to strike the target area). This printed circuit card then could be inserted into a connector at the base of the sample rod in the cryogenic dewar.

During all room temperature work, great attention was paid to the current densities that the leads may be subjected to. Extreme care was exercised to avoid exposing especially the Aluminum lead to anything greater than 1000 Amps/cm² .

Finally, in comparing room temperature impedance measurements with those impedance measurements done at liquid helium temperatures, normally the junction exhibited no more than a 10-20% impedance change. Anything more than that typically indicated a poor silver paint attachment.

3.2 Cryogenic Apparatus and Optics

Most of the experiments were performed while the junctions were at or below liquid Helium's boiling point of 4.2°K. All the experiments done at cryogenic temperatures involving laser irradiation were performed at or below the lambda point of 2.18°K to ensure optical clarity. The dewar used in this research was a product of Andonian, having a liquid Helium/sample chamber volume of 3 liters, surrounded by a vacuum space, which is again surrounded by a liquid Nitrogen thermal shroud chamber, which is finally surrounded by yet another vacuum space. All vacuum spaces were evacuated to about 10⁻⁷ Torr using a diffusion pump. The Andonian dewar was fitted with an extension that tailed about 12 inches below the 3 liter section. It is into this tail section that the sample rod with the substrate, junction and printed circuit card were inserted. Once the liquid Helium was added, a total experimental run time of about 6-7 hours could be expected, prior to "burn-out" of the liquid helium (this is to include pumping on the He section with a rough pump to reduce the temperature). All temperature measurements were made using a Lake Shore silicon diode.

Once in place, the junction could be targeted with the lasers through either of two pairs of quartz windows (two windows in the front, and two in the rear), each pair consisting of one room temp "warm" window between atmosphere and the vacuum chamber, and a liquid helium "cold" window, between the vacuum chamber and the sample area. The sample rod, and thus the substrate, could be rotated through 360°; and, with a micrometer affixed to the top of the sample rod, the height (relative to the optical plane) could be adjusted. Horizontal alignment and adjustment was obtained by moving the final mirror and final focusing lens in unison (Figures 12 and 13).

Using an Argon-ion laser that was displaced from our lab necessitated the use of a fiber optic cable in order that we may have access to the needed light. The wavelengths used were the six strong lines between 4579Å and 5145Å. The beam profile was gaussian, ensuring a minimum focal spot on the junction -- approximately 3-5 μm . To avoid intra-lens interference, all lenses were AR coated. Focusing of the beam onto the junction and "navigating" the focal spot around junction's area was accomplished using a combination of techniques. Several direct optical viewing options were tried to no great level of success. Finally, by simple use of a clean, white "screen" placed behind the tail section, one could view the transmitted light and the resulting junction's shadow. It was easy to determine from this shadow's image when the focal spot was not on the junction, and approximately whether or not the beam waist was actually on the junction. At this point, all adjustments were performed with reference to the electrical signals obtained.

Finally, a pair of polarizers were placed in the beam path (after the pin diode sensing point) in order that the power and polarization could be adjusted. All power readings were taken CW after the polarizers and prior to

the first of the two final mirrors, and the correlation factor was determined for the corresponding power at the junction's location. The data were corrected using this calibration.

3.3 Photoemissive Barrier Height Determination Arrangement¹⁰

Figure 12 outlines the experimental arrangement for the oxide's energy barrier height determination. These data were obtained strictly at room temperature, and as a result the thermal contributions had to be taken into account. The output of the Ar⁺ laser was tuned to a single line, and was then focused onto the junction (again, all power measurements were taken after the polarizers and while CW). A mechanical chopper was placed in the beam path at the focal point of two equal achromatic planoconvex lenses, providing a 70 μ sec pulse with a rise time of 3 μ sec, and an illumination rep rate of 38 Hz. The junction's response at the beginning of the pulse was determined by extrapolating the signals taken at 15 μ sec and 60 μ sec after the pulse was initiated by using a two-channel boxcar with a 1 μ sec gate width set to average 300 samples. The pulse initiation was determined by a Thor Labs silicon pin diode which was impedance matched to ensure a faithful representation of the optical pulse shape. This arrangement allowed the determination, and thus the subtraction, of the slow laser-induced thermal response. The resulting power normalized data as a function of the bias voltage provided the information for a Fowler plot, yielding the barrier height (Figure 17).

As was determined by Elchinger [1], the examined largest changes in L and $\bar{\varphi}$ that could occur through the drastic temperature change from 300°K to liquid Helium are small (in comparison with measurement errors). Reasonably

¹⁰For the most part, this procedure faithfully follows that which is described in [32].

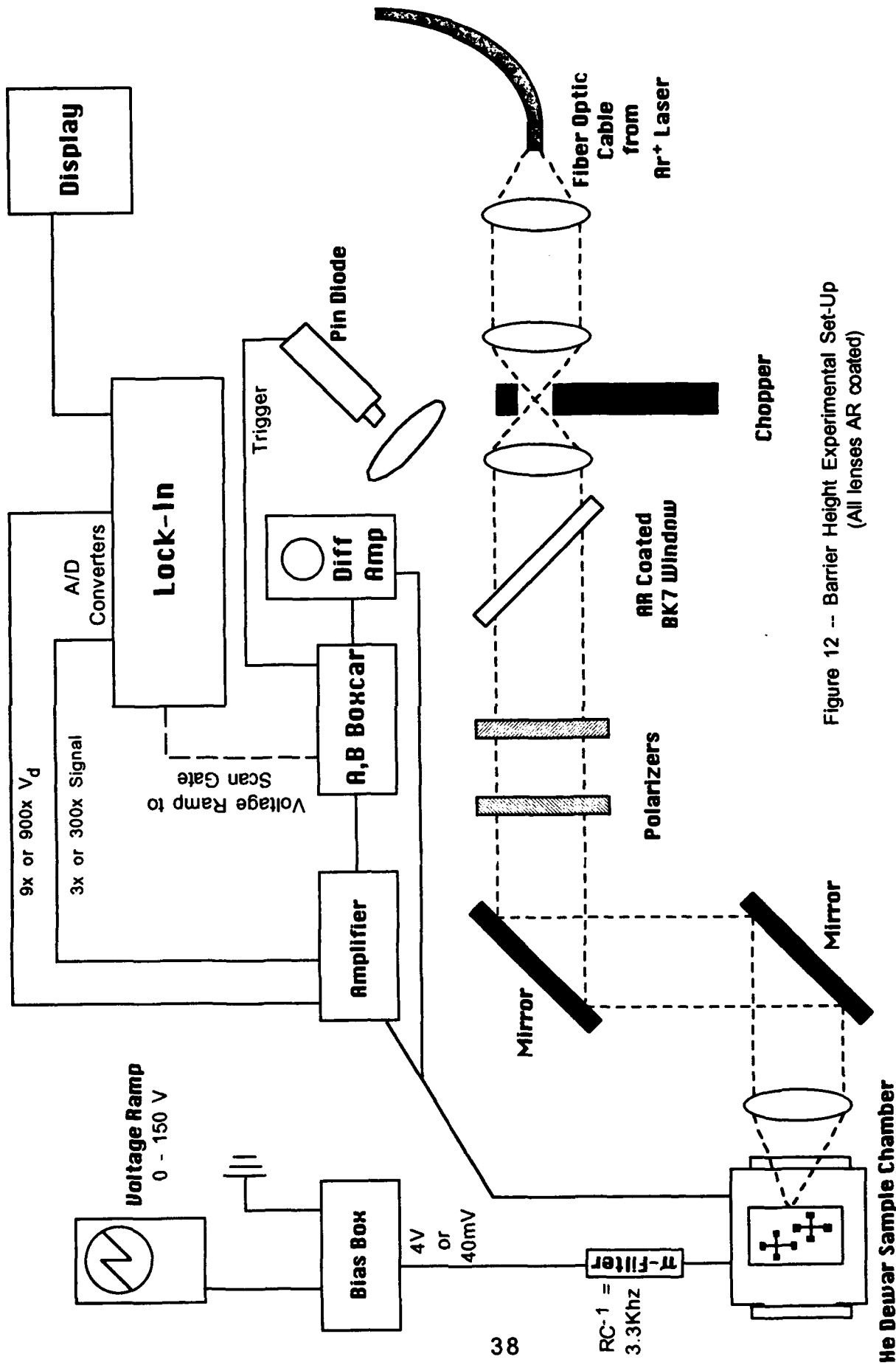


Figure 12 -- Barrier Height Experimental Set-Up
(All lenses AR coated)

small changes in R_d (no more than 20%) with temperature were ignored when determining the barrier parameters.

3.4 I-V and I''-V Arrangement

Figure 13 outlines the experimental arrangement for the I-V and I''-V data collection. All data were collected below 2.18°K, with the stronger signals being obtained at 1.7°K. Again, the Ar⁺ light was tuned to a single line and focused onto the junction. This time, though, a chopper blade was used that chopped the beam at 400 Hz, providing a pulse of 1.25 msec, while the pin diode signal was used as the lock-in reference.

For both the barrier height determinations as well as the I-V, and I''-V work, the electronics design was basically the same, requiring a bias supply, a lock-in amplifier, and a display. For the barrier height work, there were an additional two stages of amplification that the I-V work did not have (see Figure 12). In short, the junction's response was first amplified by a Tektronics 1A7A differential amplifier, which was then fed to the boxcar. Aside from that, the two arrangements were basically the same.

The 0-150V bias voltage supply was first fed into the Bias Box (Figure 14), which incorporated an operational amplifier driven feedback loop to ensure voltage control when the junction resistance changed dramatically with bias. In addition, a series current limiting resistor was included at the output. This resistor was made variable so as to obtain the maximum signal for a given bias voltage. Reference 36 develops the second derivative detection circuitry that was basically used in this experiment, and it indicates that the ideal circuit would have the bias resistance very large in comparison with R_d , effectively making a current supply of the Bias Box. However, the resulting bias developed across the junction is very small. At

the other extreme, if the bias resistance is too small, it ends up loading the junction, again producing a small response. Consequently, the variable arrangement in Figure 14 was used. In both arrangements, a dual staged amplifier (Figure 15) was used to increase the overall signal strength and to minimize the digitization error prior to entry into the lock-in.

So as to ensure accurate measurements of the junction impedance both at room temperature and at liquid Helium temperature, 4-pole measurements were made (where possible). This permitted, in essence, cancellation of the inherent line impedance, so that in effect only the junction was being examined (see appendix 3).

Finally, electrical noise was a constant concern. An extreme amount of time and effort was expended to minimize noise. Great care was taken to avoid ground loops, establishing a common instrumental ground at the Bias Box. All wires were shielded, including the junction (by the dewar). Low band pass filters were used in the Amplifier Box (Figure 14) to help filter any unwanted signals prior to amplification. And, finally, to help filter out some extremely high freq noise that we just could not get rid of, some low pass π -filters were used at the lock-in's input which significantly cleaned our signal.

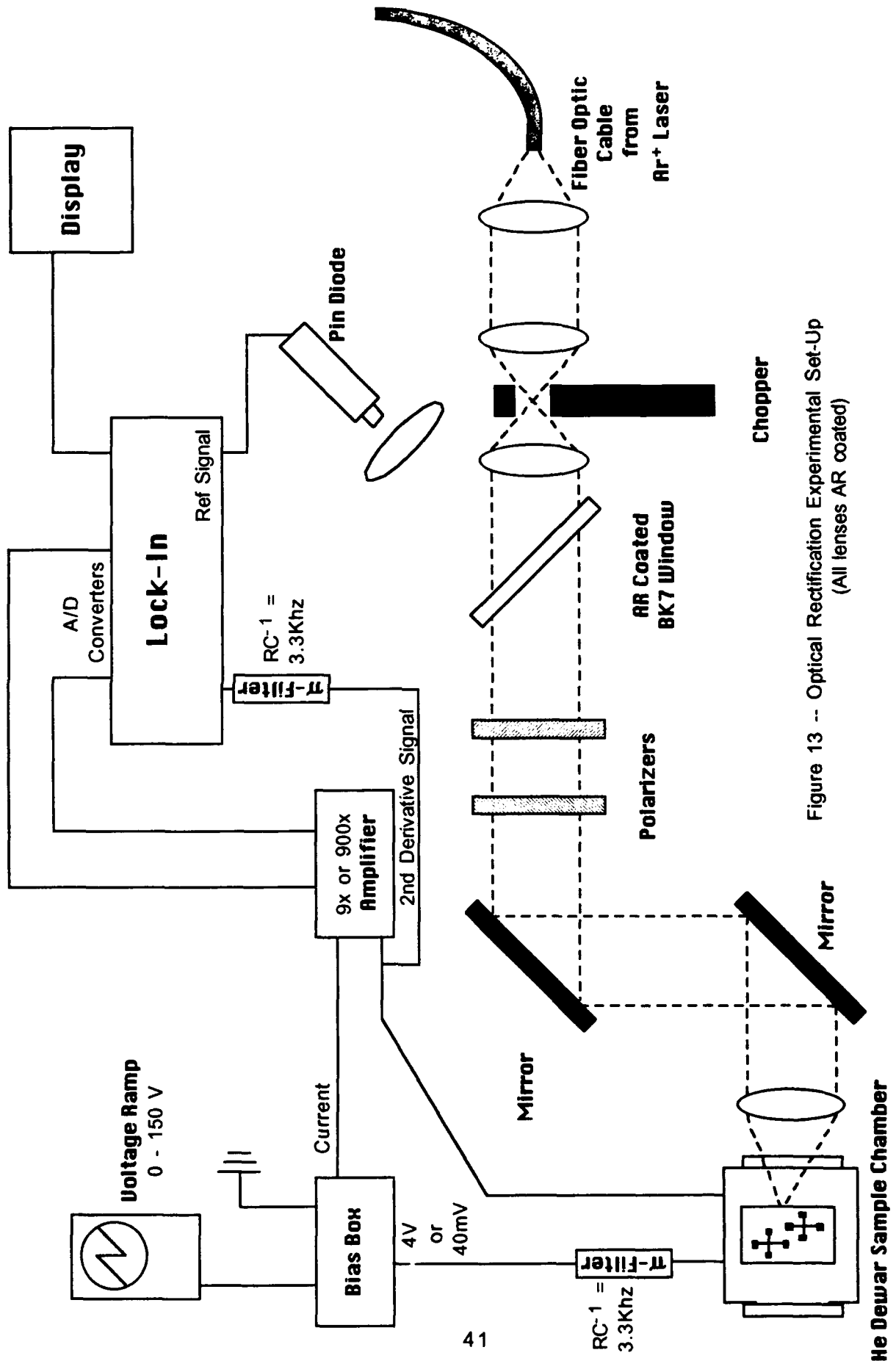


Figure 13 -- Optical Rectification Experimental Set-Up
(All lenses AR coated)

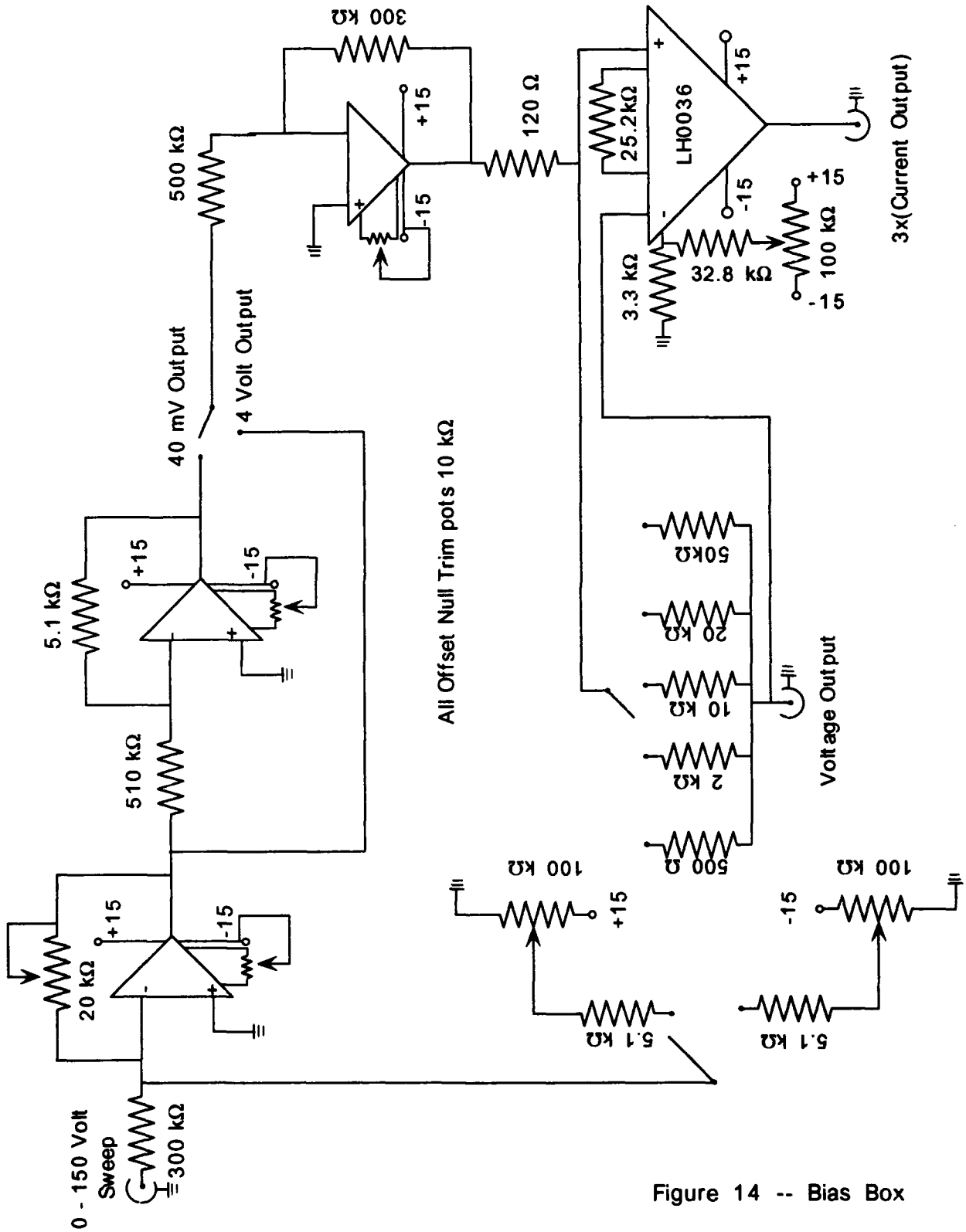


Figure 14 -- Bias Box

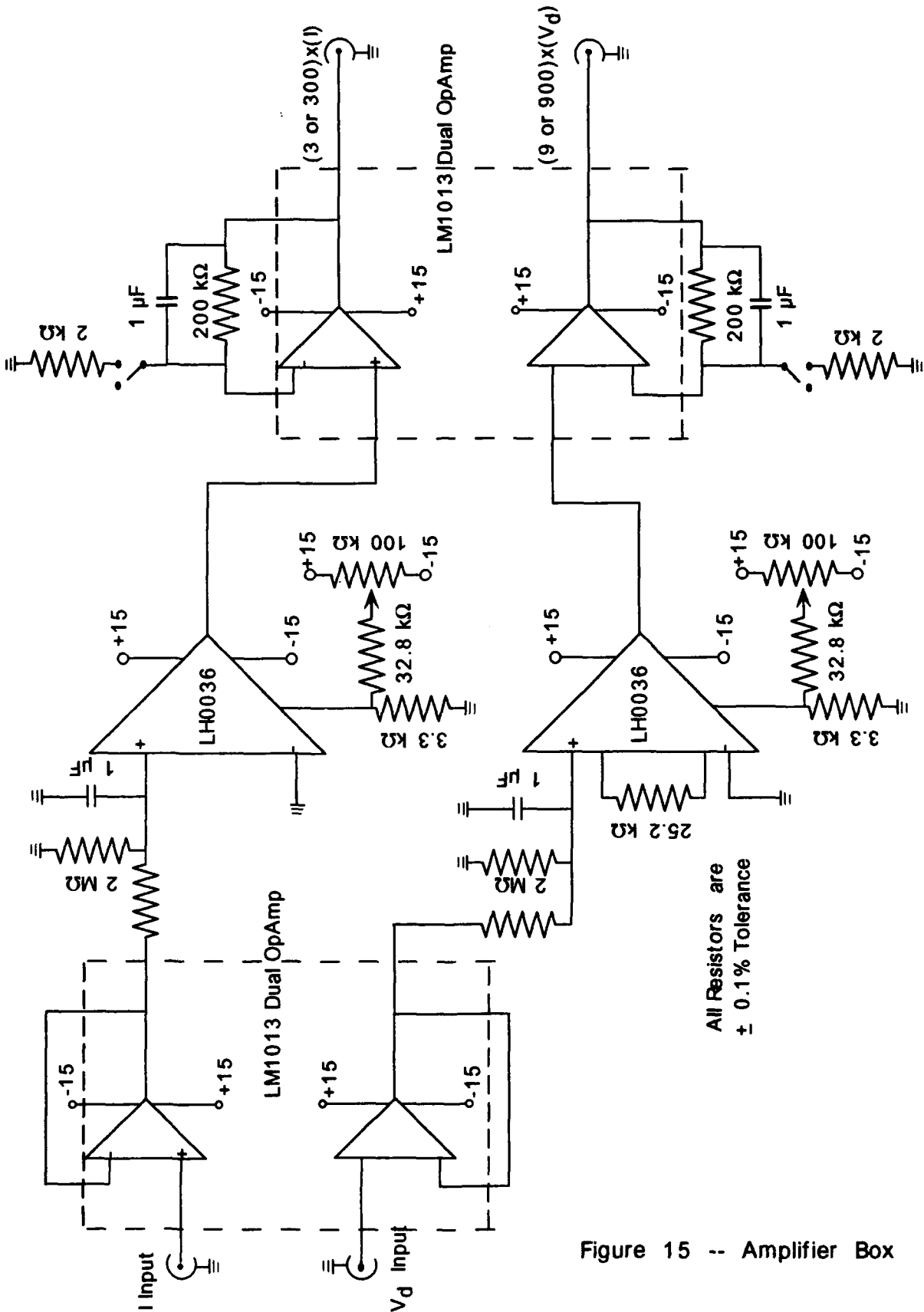


Figure 15 -- Amplifier Box

Chapter 4

Metal-Barrier-Superconductor Response

4.1 Barrier Height Determination

Several investigators [1][29][31][42] have extensively studied tunneling barrier shapes, having begun with trapezoidal assumptions. In these works the barrier height (see Figure 7) of φ_2 has been measured by photoemission over the barrier using the zero current intersection in a Fowler plot as the value of that height. In addition, most often the φ_1 barrier height could also be determined if a large enough positive bias was applied to the metal on that side. Due to the dimensions used in this work, the necessary bias would have resulted in a current density in the Aluminum leads that would have been risky at best, and damaging at worst. Consequently, this necessitated calculating the parameters of L and φ_1 from capacitance measurements, once φ_2 was known, using equation (2.4.13), and the definition $\bar{\varphi} = \frac{\varphi_1 + \varphi_2}{2}$.

By observing the photo-induced tunneling currents (PITC), φ_2 was determined to be 1.86 eV. Figure 16 shows a typical junction's room temperature PITC response to several wavelengths of light. From this data, it is then possible to take $\sqrt{J_{P.E.}}$ and plot it against $h\nu$. The resulting Fowler plot of Figure 17 permits a best straight line fit extrapolating to the $J_{P.E.} = 0$ point to determine φ_2 .

Assuming that the junction forms a parallel plate capacitor, then from a capacitance measurement and

$$R_d C_d = \frac{\epsilon \epsilon_0 a}{L} R_d = 8.85 \times 10^{-14} \frac{\epsilon a R_d}{L} \quad (4.1.1)$$

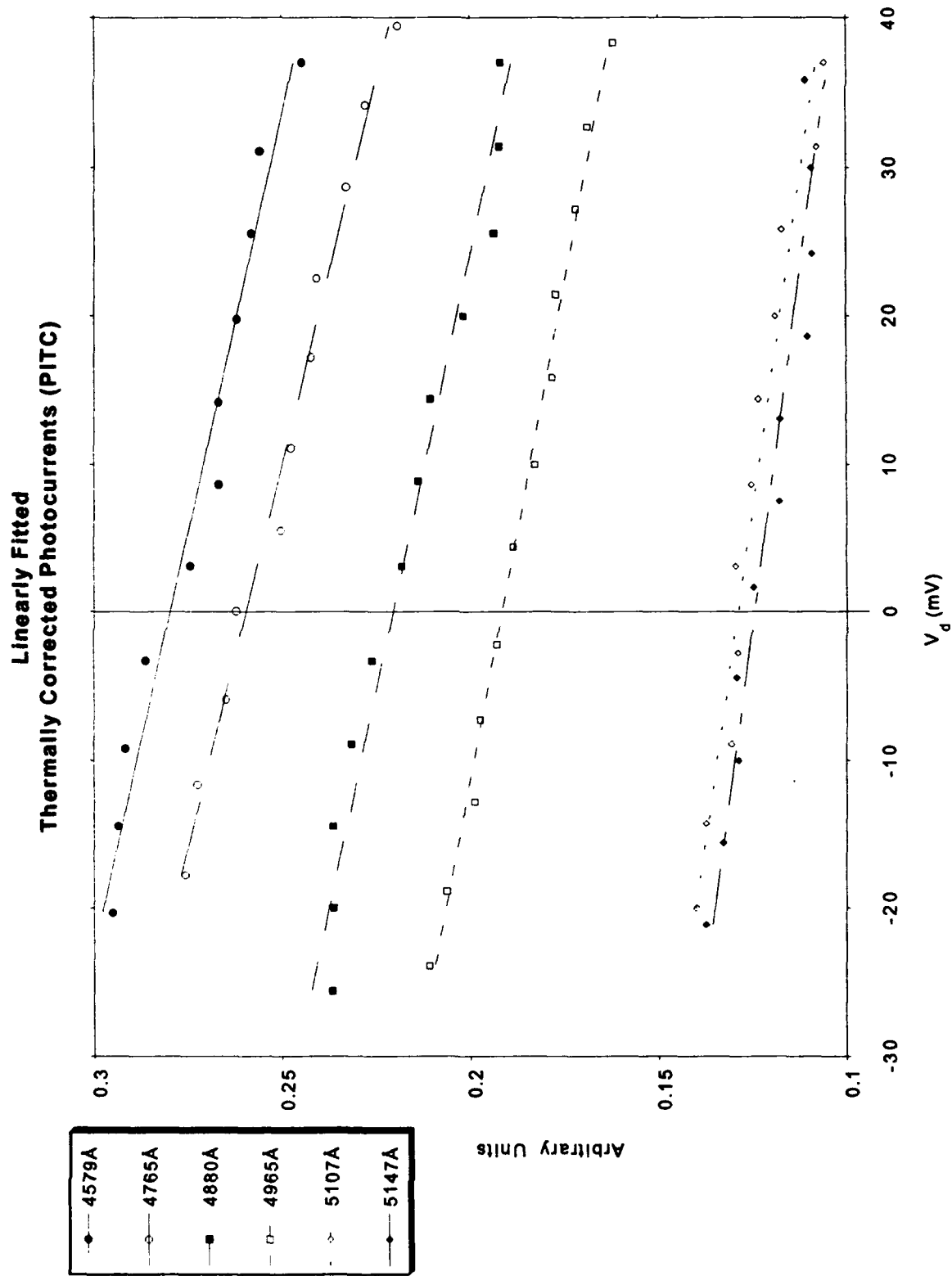


Figure 16 -- PITC versus V_d

Fowler Plot ϕ_2 Barrier Height Determination

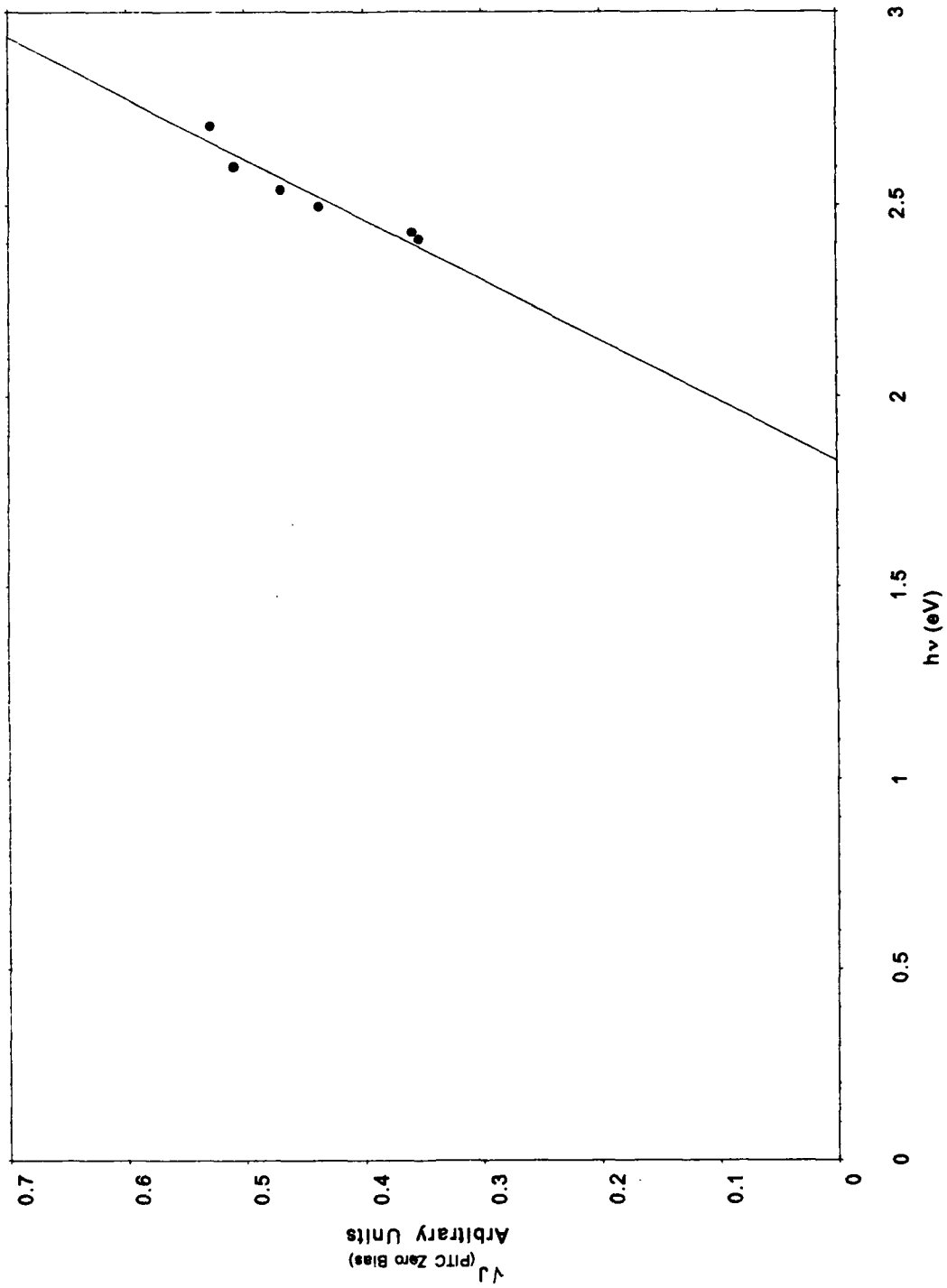


Figure 17 -- Fowler Plot to Determine Barrier Height

it is possible to determine L . Here, these units permit R_d to be in ohms, L to be in Å, and a to be in μm^2 . The dielectric constant, ϵ , has been studied by several investigators and has been determined to be 8 [1][18][31][35][42]. For resistances on the order of about 7 kohm, the capacitance was between 70-80 pF. This typically implied an oxide layer thickness of about 14.5 Å.

Through equation (2.4.13), and with L and φ_2 determined, this leads to $\bar{\varphi} = 1.74$ eV and thus $\varphi_1 = 1.62$. For the most part, then, the trapezoidal tunneling barrier has been characterized.

4.2 Photoemission and Thermal Responses

All of the above barrier parameter determinations were accomplished at room temperature. From Figure 16, it is possible to see that there is a sizable PITC. In fact, at this ambient temperature, it is the PITC that dominates as can be seen by observing Figure 18, the 70 μsec laser pulse at a bias voltage of -250 mV. The sloping top of this pulse is due to the thermal heating of the junction. Obviously here, the thermal contribution to the entire signal is easily dominated by the PITC.

However, once these junctions are cooled to liquid Helium temperatures, the PITC becomes less significant, and is easily dominated by the thermal signal. This is quite evident in Figure 19: by illuminating the junction with 1 mW of 5145Å light, it is possible to see that at the higher bias voltages, the signal is very nearly zero (thus very little PITC contribution). In addition, since there is no point at which the curve intersects the x-axis (except for the origin), there are no inflection points indicated and, thus, at this power setting, the thermal contributions also dominate the rectified response.

Not only does this curve nicely match the "calculated" thermal response curve of Figure 9, but the theoretically predicted thermal response curves of

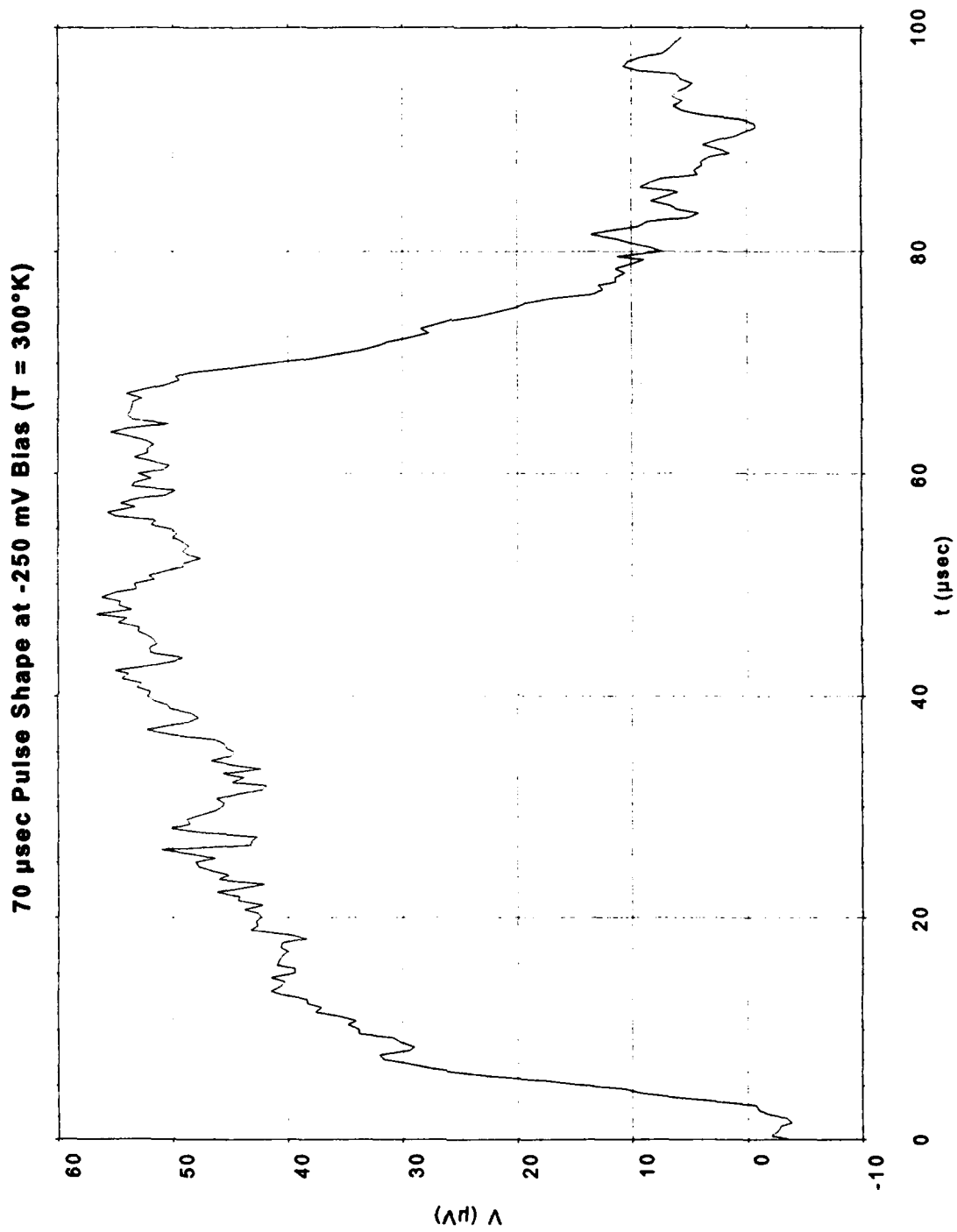


Figure 18 -- Fast Photoresponse with Thermal Response Superimposed at -250 mV Bias ($T = 300^\circ\text{K}$)

Thermal Response to 1mW of 5147A
(T = 1.7°K)

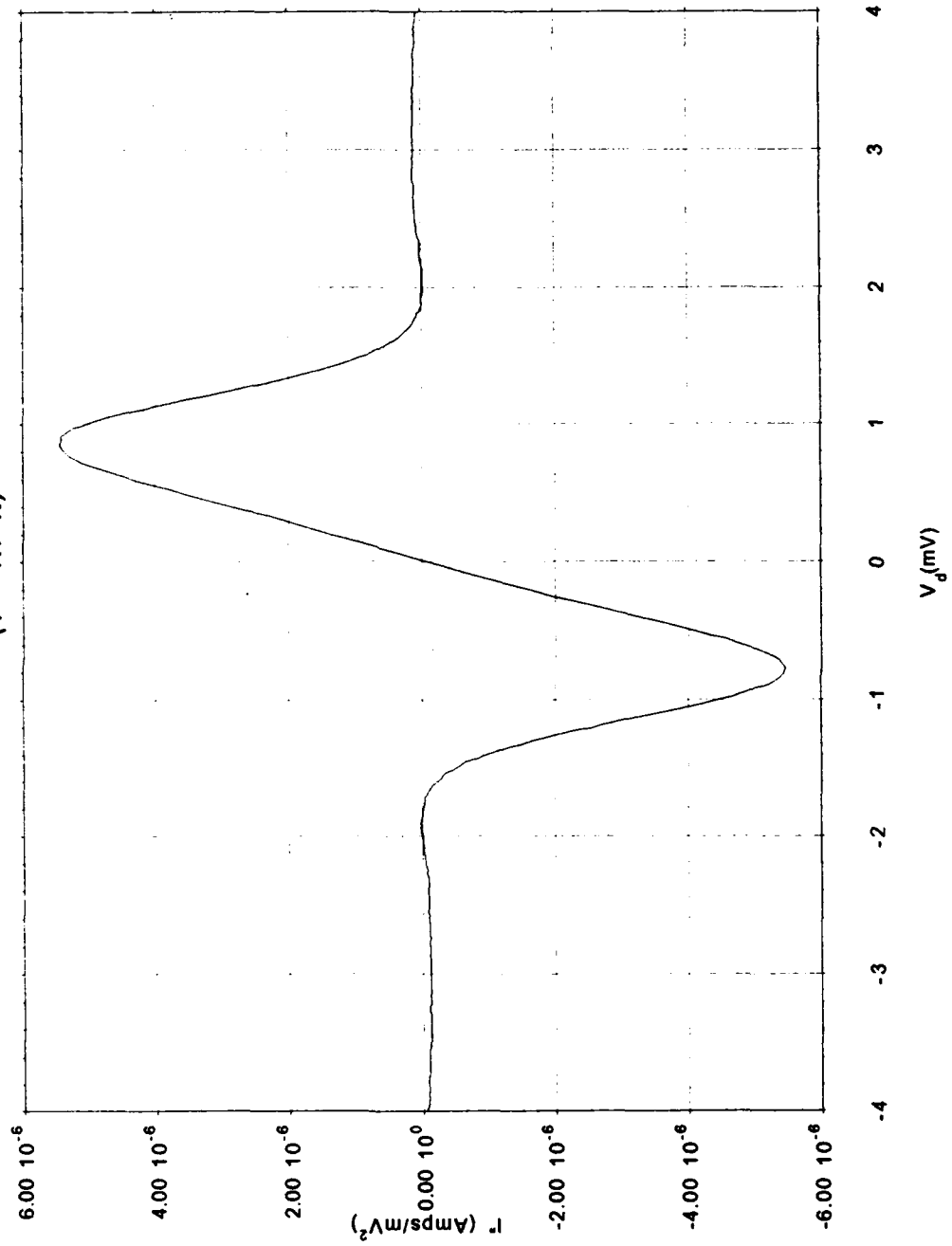


Figure 19 -- Junction's Dominant Thermal Response

Theoretically Predicted I-V Responses as the Temperature Changes

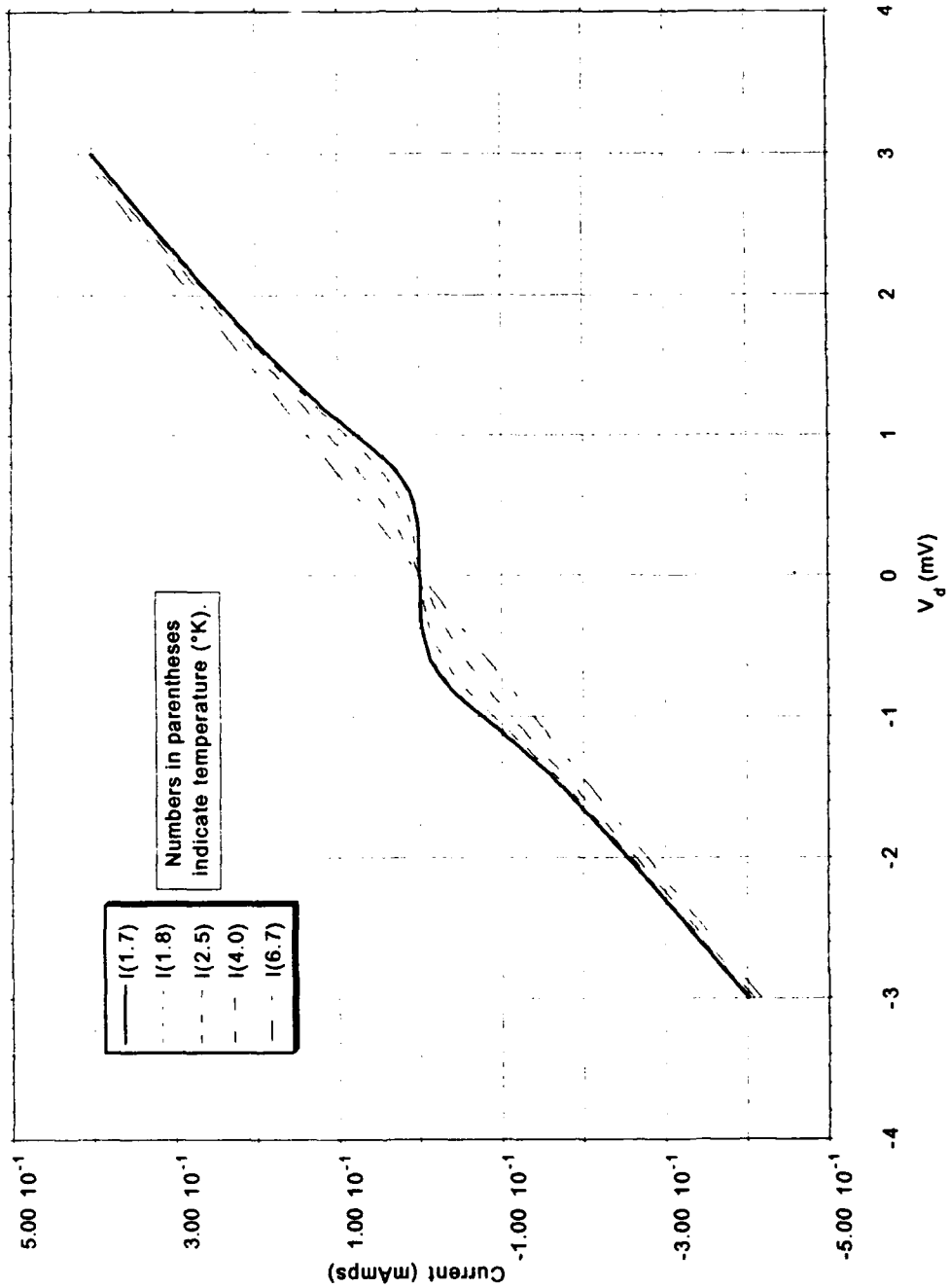


Figure 20 -- Theoretical I-V Curves demonstrating the effect of heating the junction. (Calculations based upon a 7.2k Ω junction)

Calculated 'Differential Thermal signals'

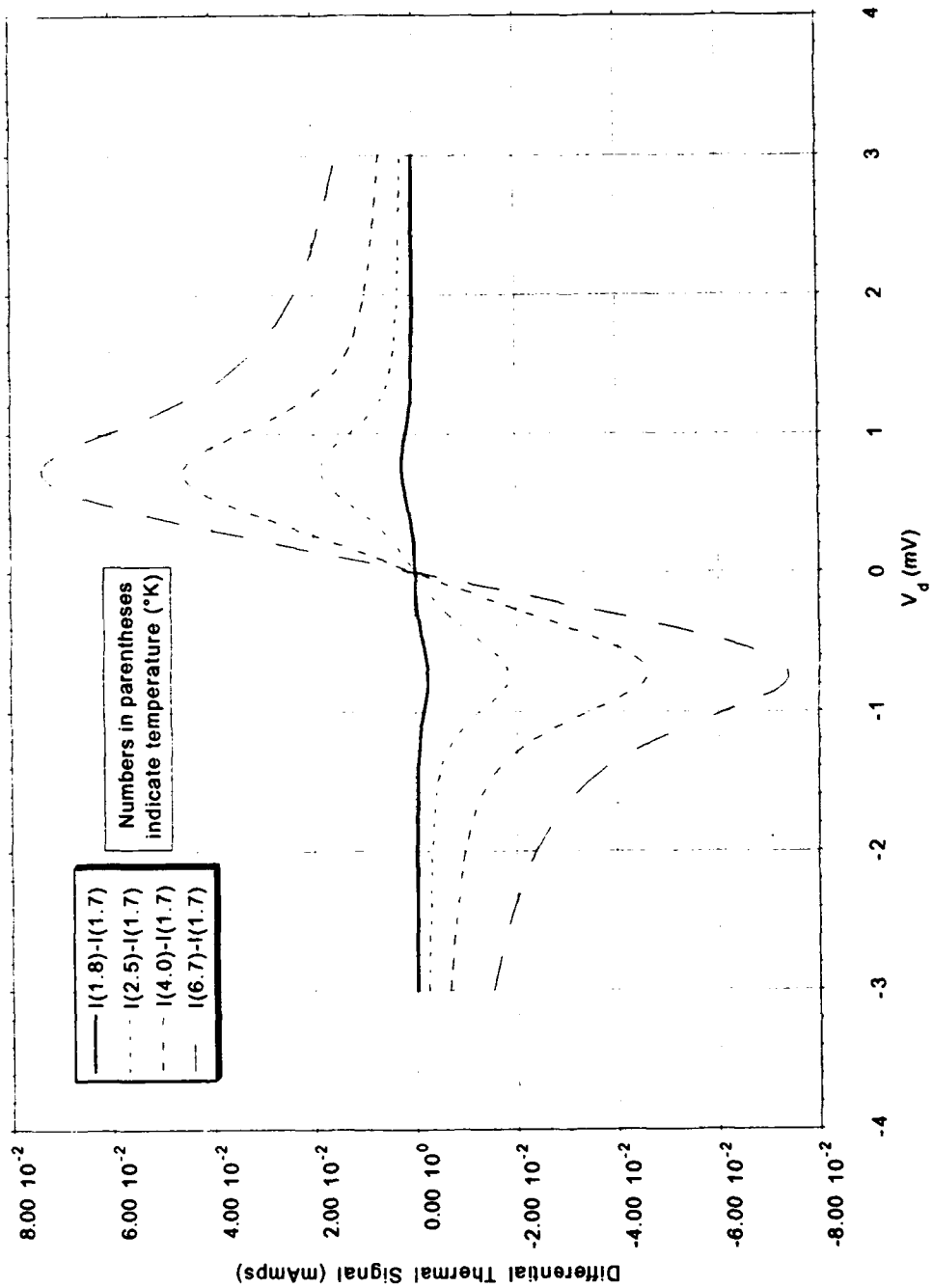


Figure 21 -- Theoretical Calculations of the Differential Thermal Contributions

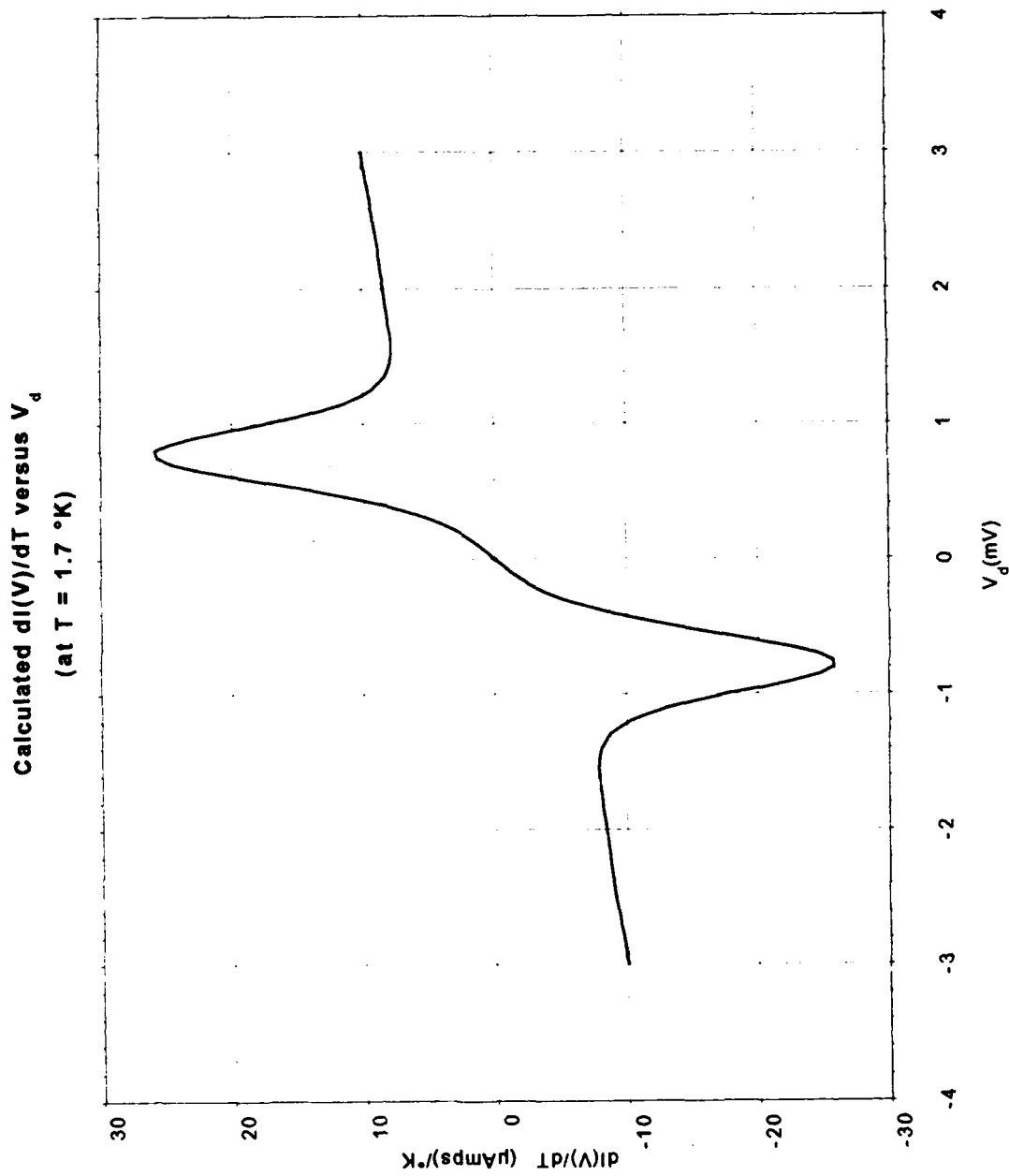


Figure 22 -- $dI(V)/dT$ of theoretical I-V curves, showing that the infinitesimal differential temperature contributions show no inflection points in I-V.

Figure 20 and Figure 21 support the general trace shape as well. The signal arising from the change in temperature of the metal-barrier-superconductor caused by laser illumination is clearly different from the predicted rectified response (Figure 30). Giaever [17] showed that upon heating a superconducting junction, the I-V curve smoothly changes toward a straight line, the slope of which represents the normal junction's high bias conductivity. Since the higher temperature curve(s) (Figure 20) never intersect the unilluminated, lower temperature curve, there can be no response that changes sign (Figure 21 and Figure 22). What this indicates, then, is that the thermal response signal can never demonstrate that the original I-V curve has an inflection point and, thus, is fundamentally different from the rectified response. In addition, this does imply, though, that the thermal contributions will alter the relative peak ratios from that predicted by theory. To put a final nail in the thermal coffin, all of the above thermal examinations have been carried out on finite temperature changes. Figure 22 displays the $\frac{dI(V)}{dT}$ curve (for an infinitesimal temperature change) of equation (2.3.5) taking into account the temperature dependence of the superconducting band gap via the BCS relation. Clearly, this shows no inflection point as well.

However, this does not yet explain why the photoemissive signal has vanished at the liquid helium temperatures. A well known characteristic of metals is that when the metal is cooled, its reflectivity increases. This is due to a reduction in the effective skin depth. For good conductors, the skin depth, δ , can be written [43]

$$\delta = \frac{c}{\sqrt{2\pi\mu\omega\sigma}} \quad (4.2.1)$$

where c is the speed of light, μ is the permeability, ω is the circular frequency of the impinging light, and σ is the conductivity (Gaussian units). From the data gathered in references [44-46] on the room and low temperature electrical conductivity of Aluminum, equation 4.2.1 yields

$$\begin{aligned}\delta_{300^\circ\text{K}} &= 64 \text{ \AA} \\ \delta_{2^\circ\text{K}} &= 6 \text{ \AA}\end{aligned}\tag{4.2.2}$$

Assuming that $\frac{\delta}{\lambda} \ll 1$, it is possible to show that the coefficient of "penetrating" light (that light which is not reflected, but in some manner scatters or interacts with the Aluminum) is

$$T_{\text{rans}} = (1 - R) = \frac{\delta 4\pi n_1}{\lambda}\tag{4.2.3}$$

where n_1 is the index of refraction for the medium from which the light penetrates the metal (in this case, either superfluid Helium, or a vacuum).

Finally, the mean free path length of the photoelectrons is vastly different at the two temperatures. This factor, too, will effect the overall amplitude of the photoemissive current. Chaverri, *et. al.*, [47] have studied Aluminum both at room temperature as well as at low temperatures. From their data, and using the Drude model to extrapolate to 2°K, the photoelectron mean free path lengths at the respective temperatures are

$$\begin{aligned}\Delta l_{300^\circ\text{K}} &= 100 \text{ \AA} \\ \Delta l_{2^\circ\text{K}} &= 950 \text{ \AA}\end{aligned}\tag{4.2.4}$$

Now, from equation (2.4.9), and from reference [29], the photoemissive current can be written as

$$I_{P.E.} \sim \frac{2\pi m e}{h^3} (h\nu - \varphi_2)^2 \left(\frac{P}{h\nu}\right) f \quad (4.2.5)$$

where P is the power of the impinging light. Expanding f,

$$I_{P.E.} \sim \frac{2\pi m e}{h^3} (h\nu - \varphi_2)^2 \left(\frac{P}{h\nu}\right) \sigma \tau (1-R) \quad (4.2.6)$$

where σ is the cross section for photogeneration of hot electrons, and τ is the mean free time of photoexcited electrons. Rewriting the above equation in terms of mean free path lengths, and Fermi velocities, v_f ,

$$I_{P.E.} \sim \frac{2\pi m e}{h^3} (h\nu - \varphi_2)^2 \left(\frac{P}{h\nu}\right) (\alpha n_e) \left(\frac{\Delta l}{v_f}\right) (1-R) \quad (4.2.7)$$

where α is the light absorption coefficient, and n_e is the number of electrons illuminated. Finally, this can be rewritten in terms of the skin depth, δ_T , and the electron density, δ_{n_e} , as

$$I_{P.E.} \sim \frac{2\pi m e}{h^3} (h\nu - \varphi_2)^2 \left(\frac{P}{h\nu}\right) (\alpha) [\delta_T (\text{volume illuminated}) (\delta_{n_e})] \left(\frac{\Delta l}{v_f}\right) (1-R) \quad (4.2.8)$$

Measurements were made at both room temperature and at superfluid Helium temperatures at the extreme ends of the bias voltage ramp. It was found, using the same light intensity at both temperatures, that the overall reduction in photoemissive signal strength was reduced by a factor of about 20 when at liquid helium temperatures.

Now assuming that δ_{n_e} , α , v_p , φ_2 and the probability for tunneling remain unchanged between the two temperatures, then the relative photocurrent intensities will be

$$\frac{I_{2^\circ\text{K}}}{I_{300^\circ\text{K}}} = \frac{(1 - R_{2^\circ\text{K}}) \delta_{2^\circ\text{K}} \Delta_{2^\circ\text{K}}'}{\Delta_{300^\circ\text{K}}'} \approx \frac{1}{10} \quad (4.2.9)$$

which is not a bad correlation with the overall reduction seen here. And, considering that the photoemissive contributions are more intense at the higher bias voltages, this bodes well for the lack of any visible contribution from the photoemissive current during the rectification studies, since these data were collected at voltages near zero bias (± 5 mV).

4.3 Fermi Level Modulation at Optical Frequencies -- Rectification Data and Response

Armed with the above appreciation, it is now possible to show that when illuminating the metal-barrier-superconductor junction with the proper light intensity, the responses seen are dominated by rectification due to the modulation of the Fermi level at an optical frequency.

From equation (2.3.5), $\frac{d^2 I(V)}{dV^2}$ has been calculated and displayed in Figure

23. Again, note here that the significant qualitative difference between the rectified and thermal signals is that the thermal response does not change sign and thus does not indicate an inflection in the I-V curve, in comparison to the rectified response which does. Both of the curves in Figure 23 typify the metal-barrier-superconductor (M-B-S) junction response because of the familiar quick rise in current at $V_b = \Delta/e$, and the smooth, asymptotic behavior toward linearity at large bias. From this behavior, it is also to be

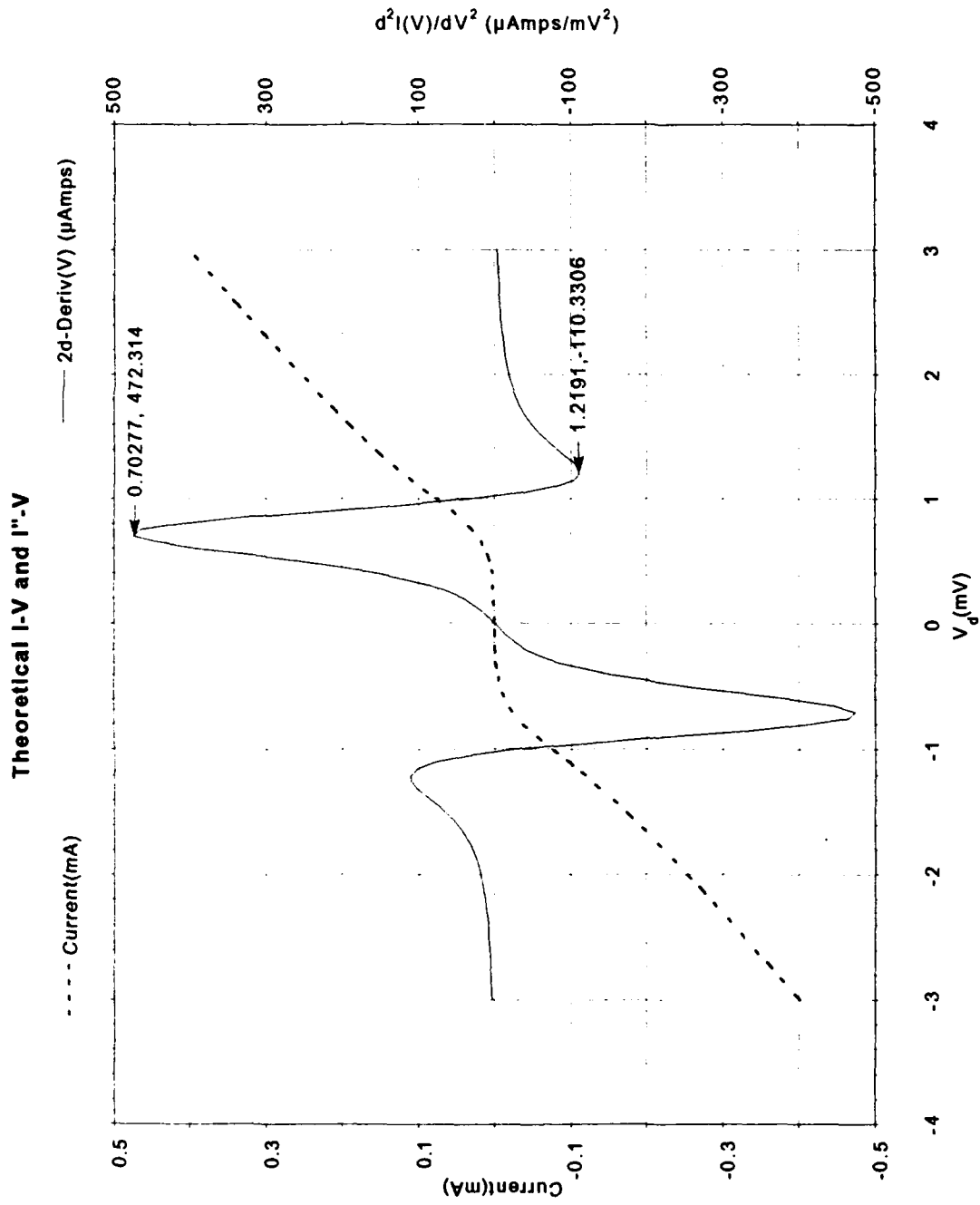


Figure 23 -- Theoretical I-V and Second Derivative Rectified Response Curves
(calculated for a 7.2k Ω junction)

I⁻-V of a Superconductor-Barrier Superconductor Junction (T = 1.3°K)

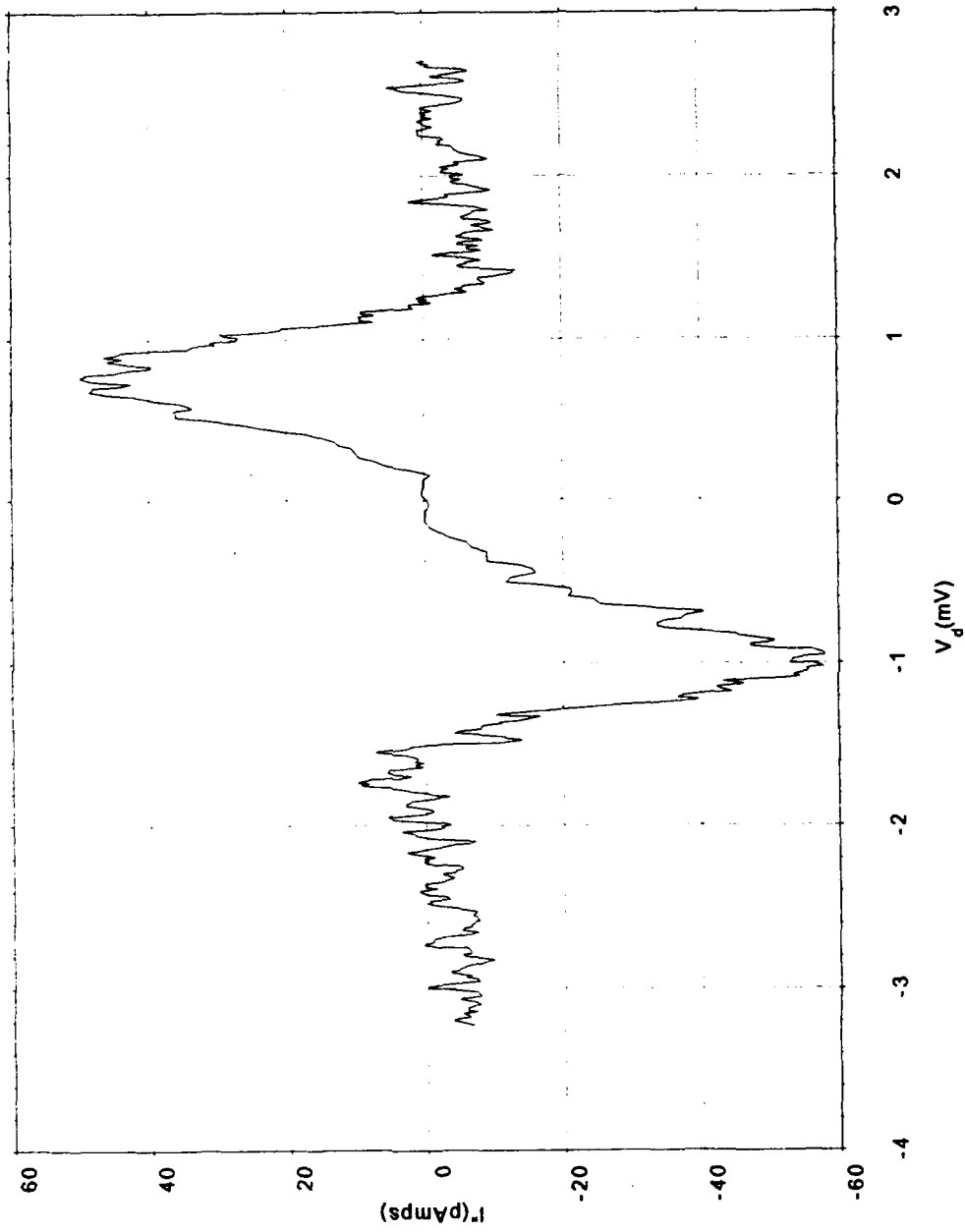


Figure 24 -- I⁻-V of a S-B-S Junction

Audio Second Derivative
(200 Hz modulation, 2mV peak-to-peak)

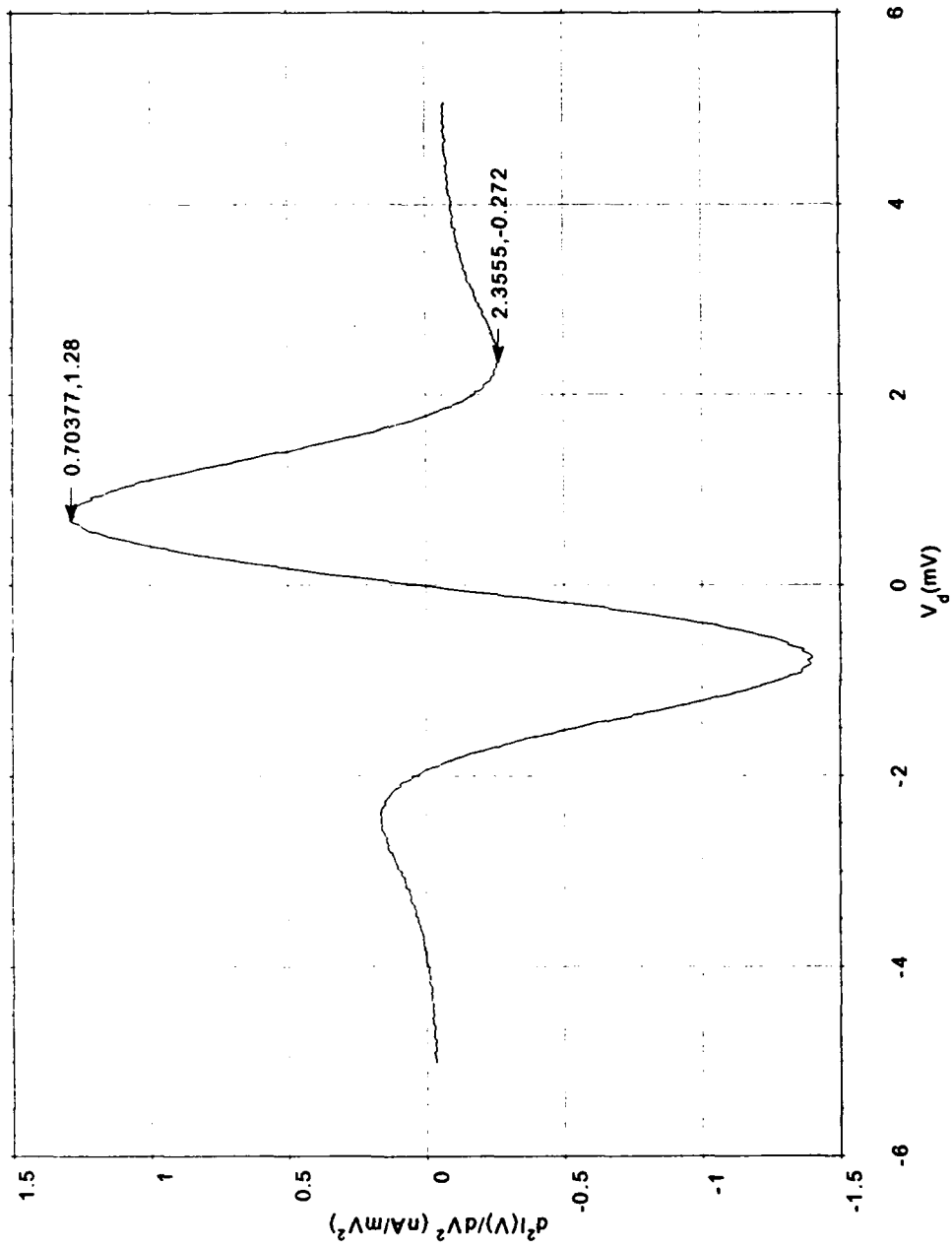


Figure 25 -- Fermi Level Modulation via Audio Frequency $d^2I(V)/dV^2$ by impressing a 200 Hz, 2mV (peak-to-peak) sine wave

determined that the junctions' responses were truly of a normal metal-barrier-superconductor response. As Giaever [17] so aptly demonstrates, the I-V and, thus the $I''(V)$ curves are vastly different when the junction is comprised of a superconductor-barrier-superconductor. Careful monitoring of the second derivative response combined with ensuring that the temperature was no colder than 1.7°K guaranteed that Aluminum remained normal. In addition, impedance measurements on Aluminum at the operating temperatures always indicated a low but finite (approximately 5-15 Ω) resistance. Finally, to illustrate the fundamental difference between a M-B-S and an S-B-S rectified response, Figure 24 clearly displays a zero slope region inside 2Δ -- consistent with the second derivative of an I-V curve for two superconductors who have no current flowing while the respective band gaps are "juxtaposed". Consequently, it was easy to ensure that the junction was truly M-B-S during the experiments.

Now in section 4.2, it was shown that although the thermal response is dominated by the rectified response (that is, the rectified response changes sign while the thermal response does not), the thermal contributions can alter the relative peak ratios. A ready means of demonstrating this is by applying an audio frequency across the junction. Figure 25 shows the rectified response of a M-B-S junction when a 2 mV (peak-to-peak), 200 Hz sinusoidal signal was applied. The resulting heating effect is minimal (but still observable), while the trace is very nearly that predicted by theory.

Note here, also, that the height of the peaks (A and B) should be affected by the temperature, through the temperature dependence of the I-V curve, as well as through V_{sinewave}^2 . Since the rectified response is linear in V_{sinewave}^2 , the ratio of A/B is not a function of V_{sinewave} , but primarily of temperature.

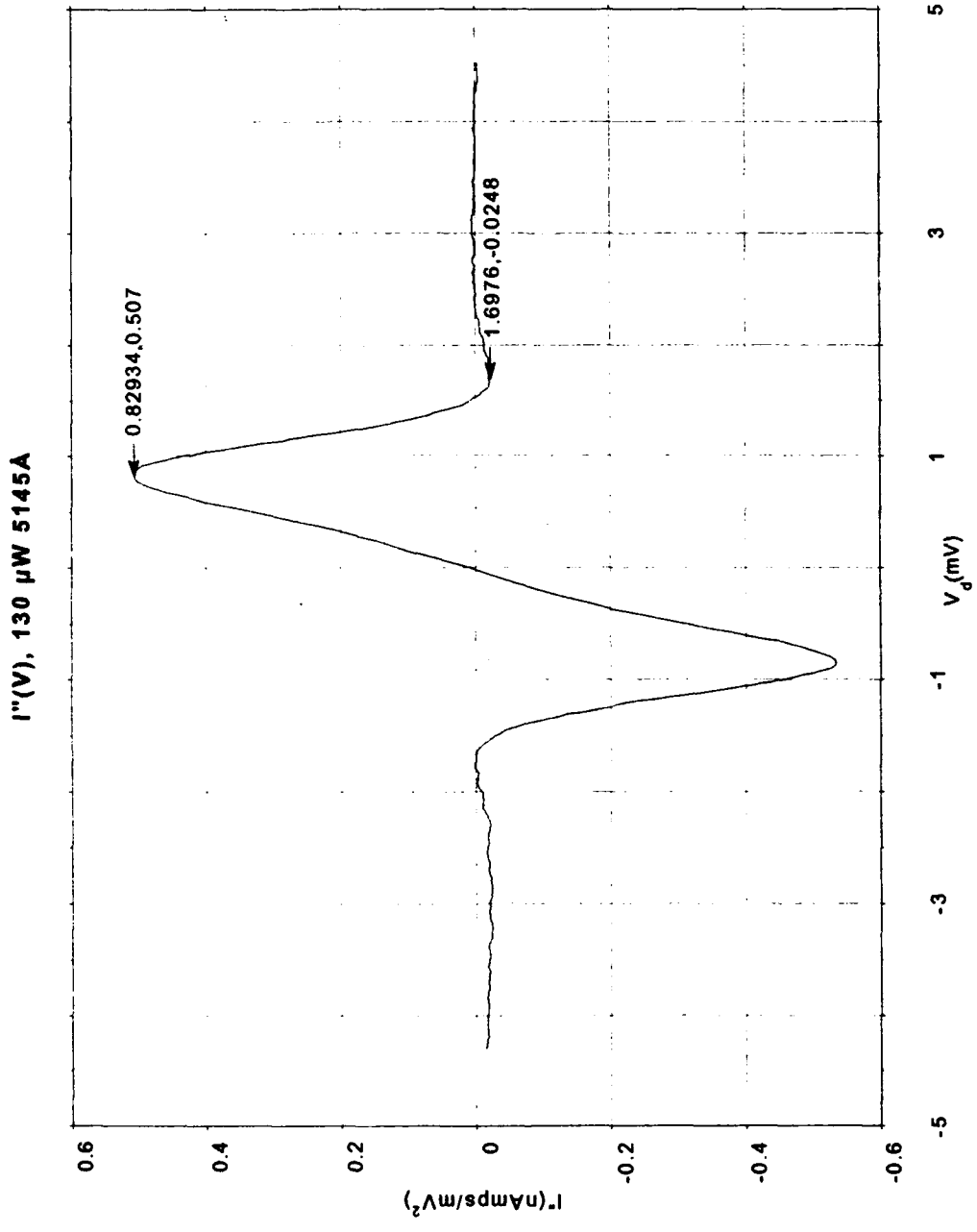


Figure 26 -- Second Derivative Rectified Response
Resulting from 130 μ W of 5145A

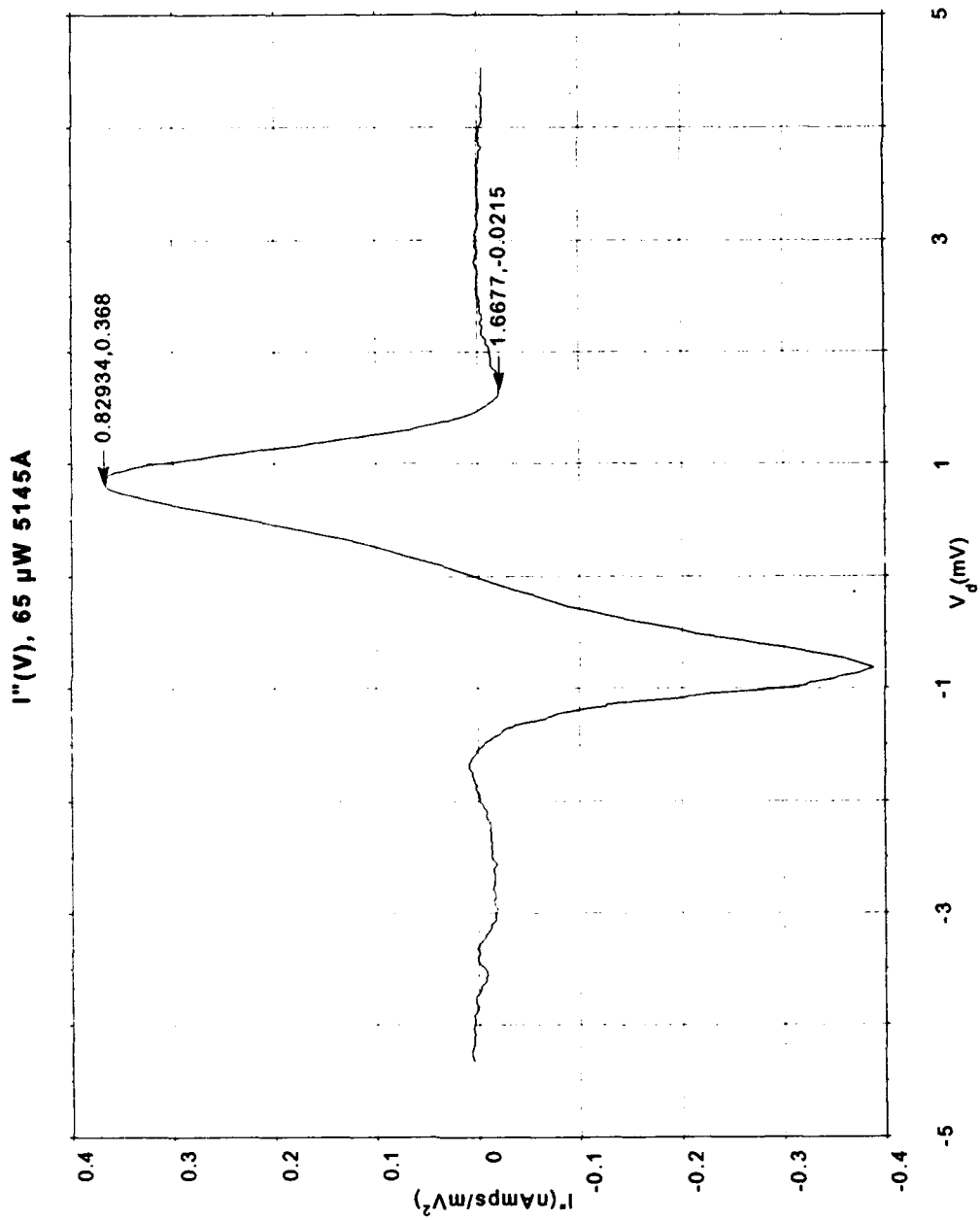


Figure 27 -- Second Derivative Rectified Response
Resulting from 65 μ W of 5145A

$I''(V)$, 40 μ W 5145A

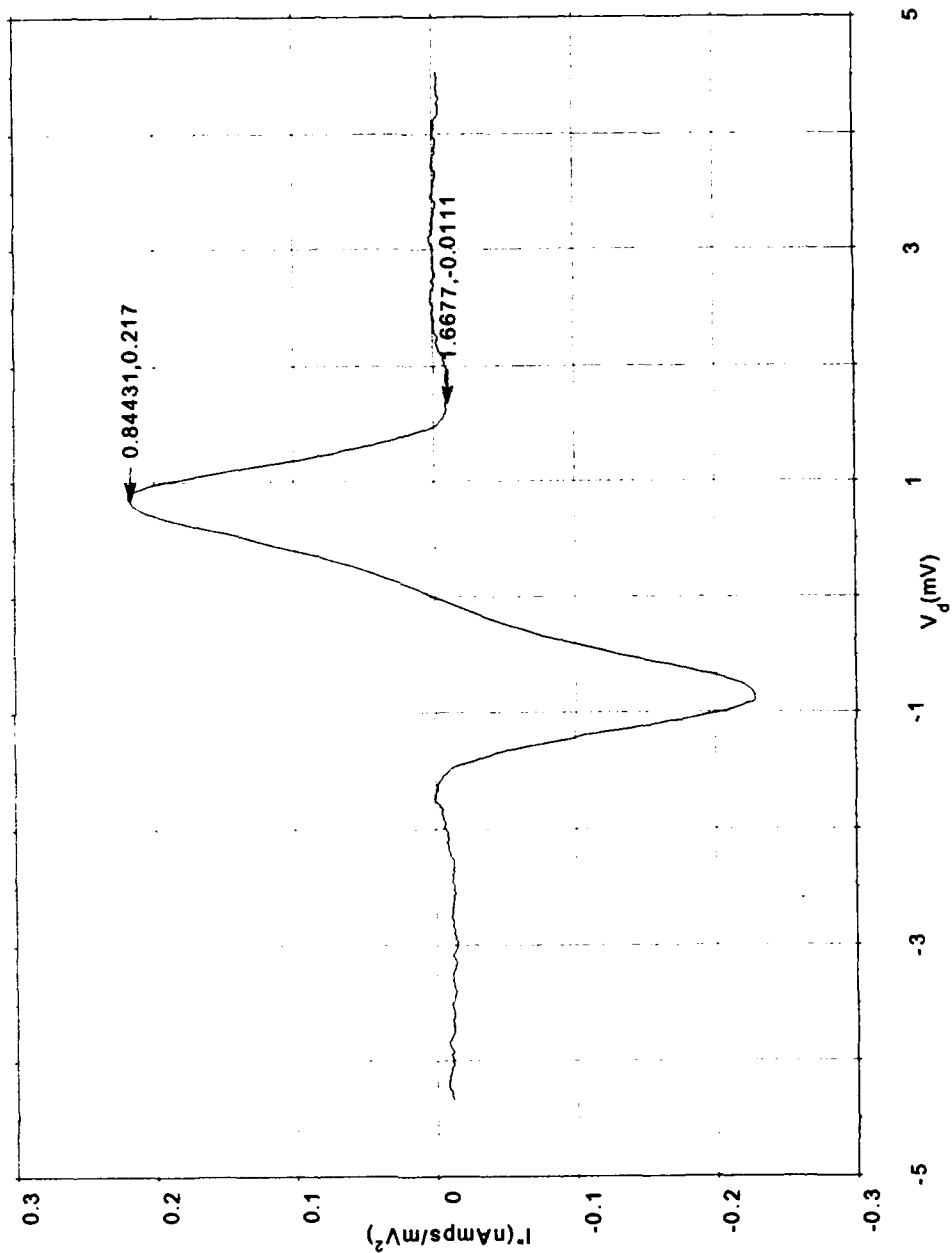


Figure 28 -- Second Derivative Rectified Response Resulting from 40 μ W of 5145A

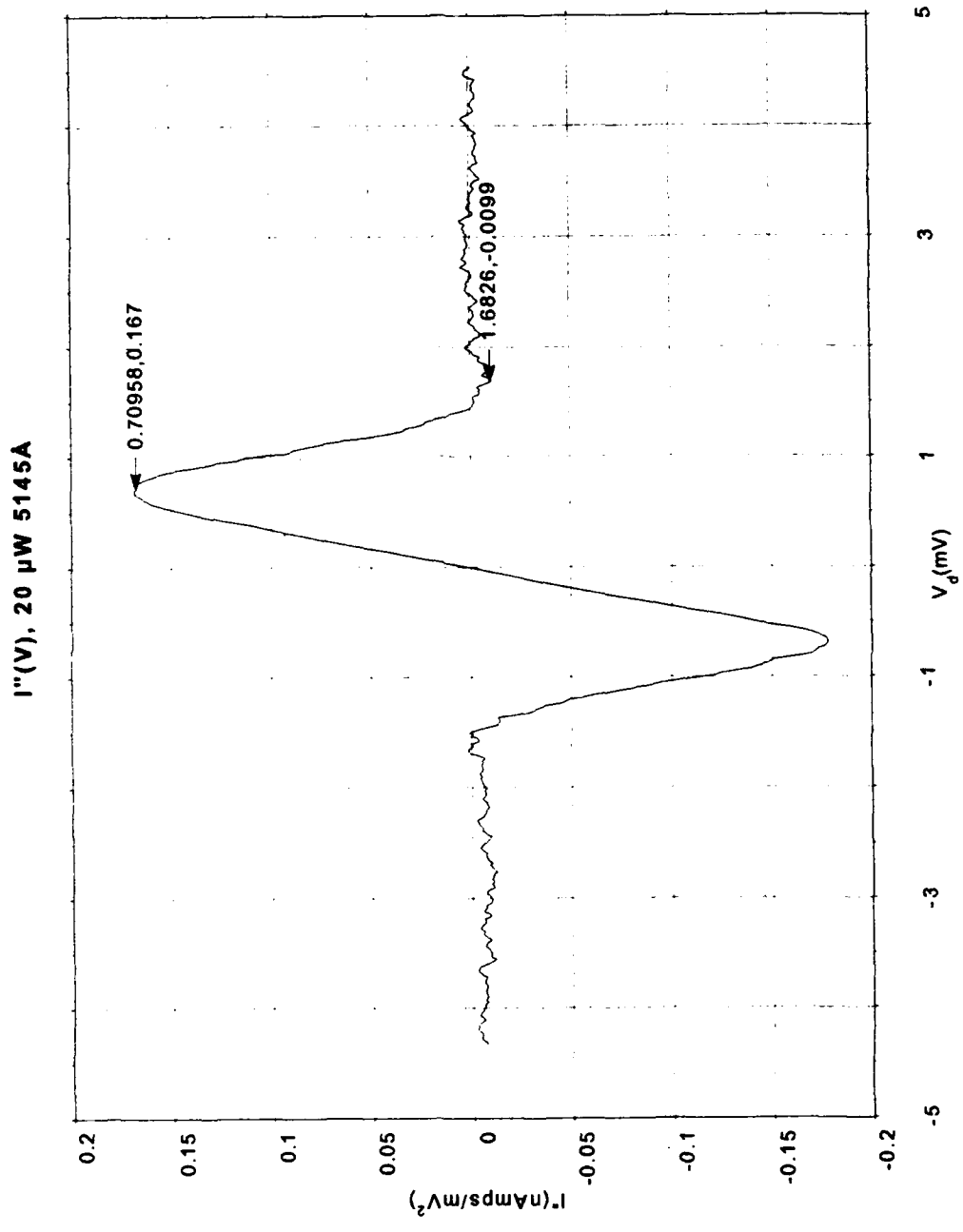


Figure 29 -- Second Derivative Rectified Response
Resulting from 20 μ W of 5145A

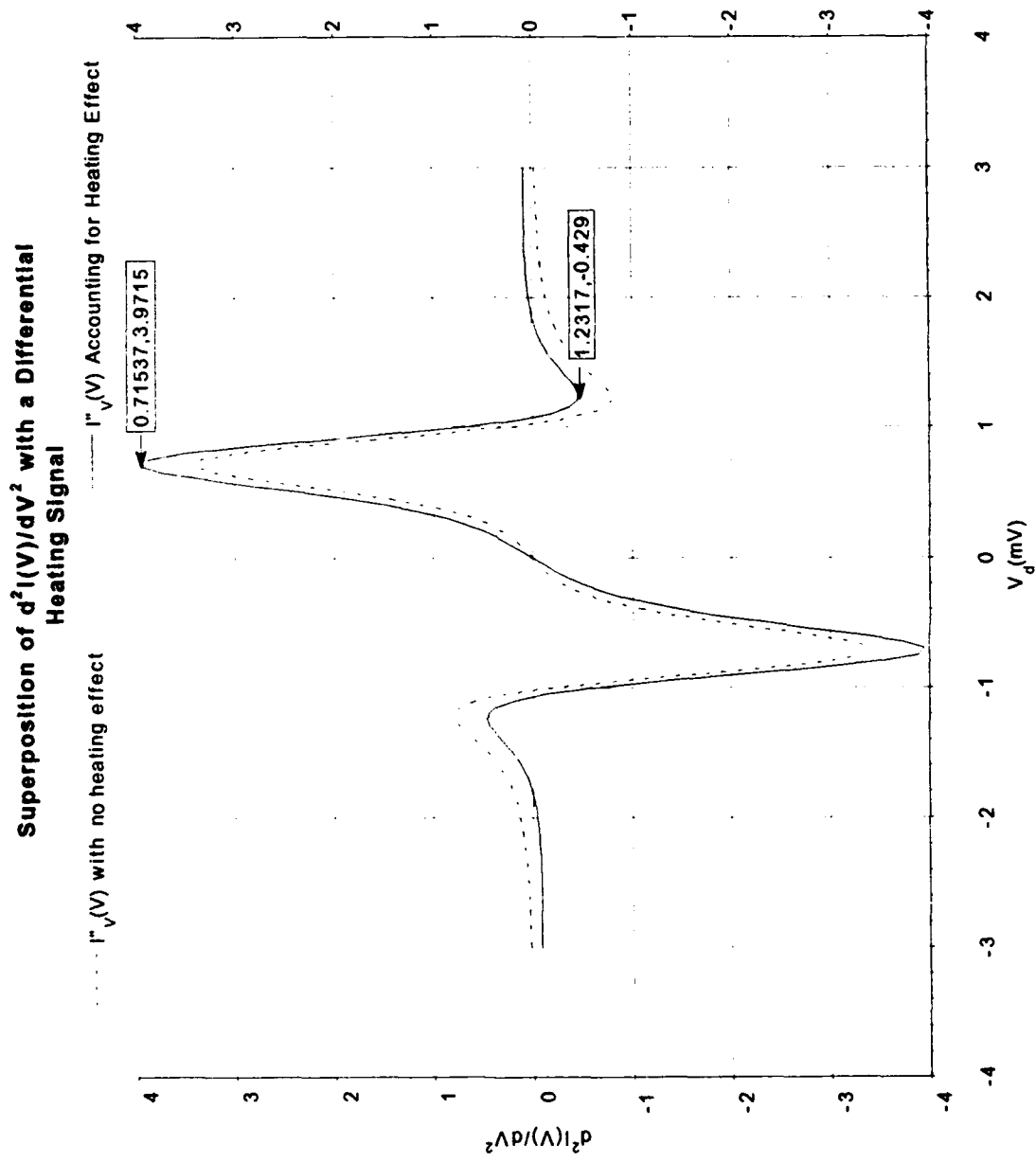


Figure 30 -- Demonstration of the Effect that the Thermal Signal Can Have on the Peak Ratios

This can be seen in the series of Figures 26-29, as the power of the laser light was changed from 120 μW to 20 μW . The ratio of A/B remains nearly constant, approximately 18:1, in this power region where the heating effect had been minimized. In addition, Figure 30 shows a theoretical superposition of the $\frac{d I(V)}{dT}$ curve on top of the $\frac{d^2 I(V)}{dV^2}$ curve. Note here that the relative peak heights approach a ratio of $A/B \approx 10:1$. Clearly this indicates that the differential thermal signal is playing a part, although an additional factor of 2 (or more) needs to be accounted for.

Elchinger [1] accomplished an exhaustive study of the response dependence upon polarization and the angle of incidence. While aware of this dependence, we only maximized the response amplitude by ensuring that there was an E-field perpendicular to the junction. However, this point is worthy of some discussion for it has been the grounds for discounting rectification via modulation of the Fermi level at optical frequencies [1]. Elchinger notes that the absorption is independent of polarization at normal incidence, while for increasing incident angle the absorption decreases when the electric vector is perpendicular to the plane of incidence. When the polarization is parallel to the incident plane the absorption slightly increases until the incident angle reaches the principle angle. Although Elchinger observed the characteristic response at normal incidence (and with a large signal response), he attributes the fact that since there is no E-field component perpendicular to the barrier that Fermi level modulation cannot occur. To this end, on an optical scale, the surface of the target area cannot be perfectly smooth and thus cannot be completely normal to the incoming light. Hence, there must be some component of the E-field which will be perpendicular to the barrier.

Finally, some discussion is warranted regarding the overall amplitude of the rectified response that is observed. Taking Figure 27 as an example, focusing the light to an area of $5 \mu\text{m}^2$, the resulting square of the amplitude of the E-field would be

$$\epsilon^2 = \frac{8\pi P}{ac} = 208 \left(\frac{\text{V}}{\text{cm}} \right)^2 \quad (4.3.1)$$

Using this value, equation (2.4.12), and the theoretical value for $\frac{d^2 I(V)}{dV^2}$ from

Figure 23 results in an expected 26 mAmps across the $7.2 \text{ k}\Omega$ junction.

Hardly the signal observed. However, taking into account the skin depth, the lead thickness (between 100\AA and 150\AA), and the resulting attenuation of the E-field that goes as $e^{-t/\delta}$, then factoring in the dielectric constant, a resulting current on the order of 0.4 nAmps could be expected. This is very nicely in the region that we were observing signals, indicating that the E-field was penetrating the Aluminum, albeit inefficiently.

In addition, it should be noted that using the conditions reported by Elchinger, it is possible to very nearly exactly theoretically model his rectified response. Assuming no heating effect at all, his Al-Al₂O₃-Pb M-B-S junction would have yielded a peak ratio of 3.7:1 (Figure 31). However, he reports a peak ratio of 7.6:1, which is nicely modeled by accounting for a heating effect due to illumination, and taking into consideration the band gap dependence on temperature (Figure 32). The significant difference in Elchinger's conditions and those in this work is that his Aluminum leads were 4 to 6 times thicker. There are indications [50] that as the Aluminum thickness diminishes to dimensions close to ours that the E-field is able to propagate longitudinally through the electron plasma. This may have the resulting effect of skewing the peak ratios as we have seen.

Theoretical Prediction of an Al-Al₂O₃-Pb M-B-S
 Junction's Rectified Response
 (T = 1.7°K)

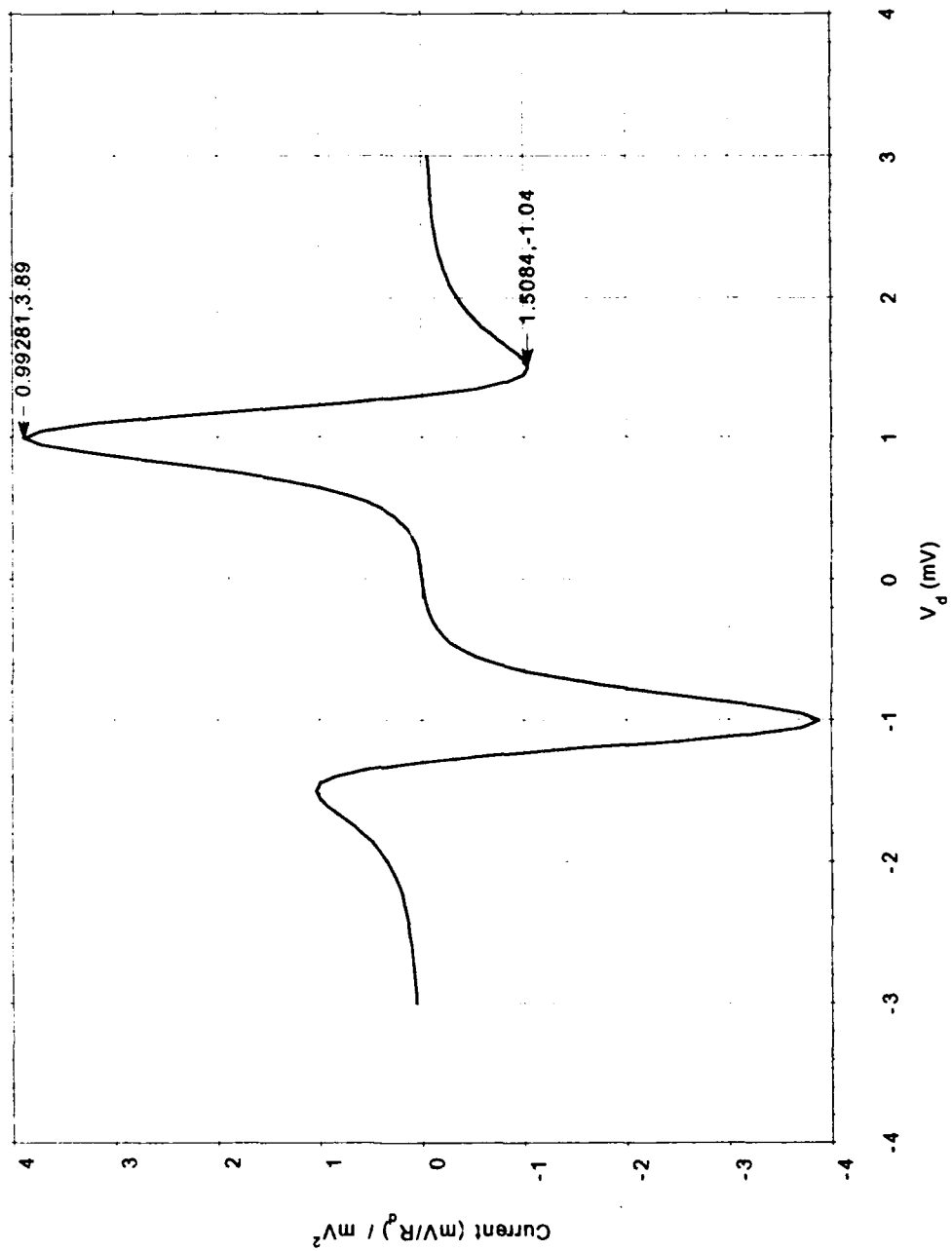


Figure 31 -- Al - Al₂O₃ - Pb M-B-S Predicted Response Without Accounting for a Superimposed Heating Effect

Theoretical Prediction of an Al-Al₂O₃-Pb M-B-S
 Junction's Rectified Response While Accounting for the Effect of Heating

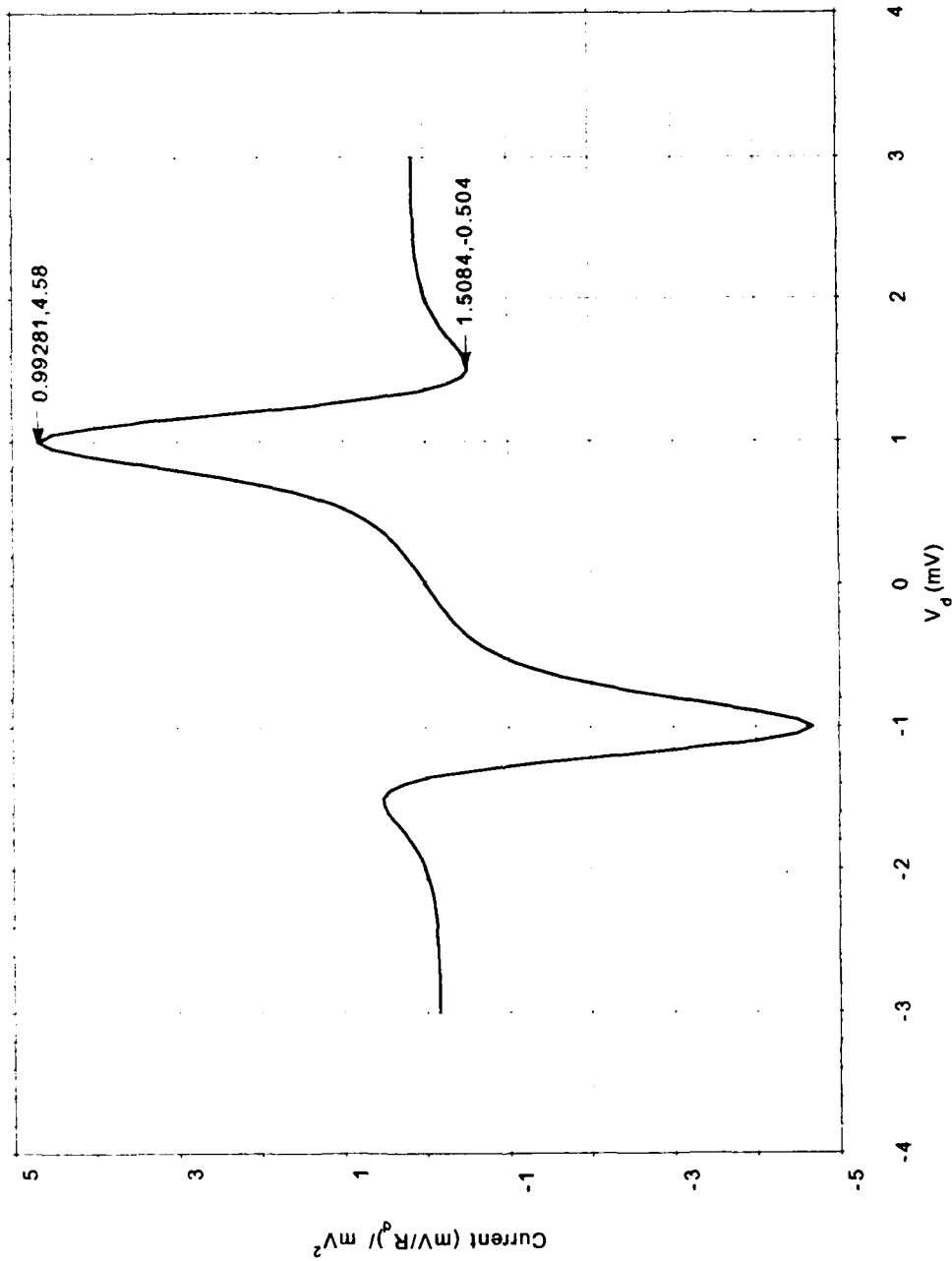


Figure 32 -- Al-Al₂O₃-Pb M-B-S Predicted Response while Taking into Account the Heating Effect ($T_{\text{ambient}} = 1.7^{\circ}\text{K}$)

Chapter 5

Future Work

As was demonstrated in the last section, rectification as a result of Fermi level modulation across the barrier dominates when the E-field couples across the barrier -- resulting in a response that traces the second derivative of the junction's I-V curve. However, the strength of this rectification signal in this work was several orders of magnitude weaker than desired or initially expected as a result of the means by which the E-field does indeed get coupled across the barrier. That is to say, once again, that the penetration of the illumination through the metal lead is a most inefficient means of accomplishing the task at hand. Better signals may be obtained through some clever and judicious techniques.

With the present state-of-the-art photolithographic fabrication techniques, it is possible to construct high-speed junctions whose dimensions are $\leq 1\mu\text{m}$. In fact, with current nano-architecture capabilities, resolutions down to 300nm are possible. At these dimensions, it is possible to see from equation (4.1.1) that the speed of this element will be significantly enhanced. Using any of a variety of geometries, the aim of the fabrication would be to integrate the high-speed junctions with optical frequency antennae resonating as a dipole. These antennae could be designed to match the junction impedance ($\sim 100\Omega$) and, as a result, would permit the coupling of the impinging E-field across the barrier at an amplitude sizably larger than the E-field produced by the edge/penetration coupling technique used in this work. Not only would this permit huge signals, and great signal-

to-noise ratios, but would also allow nanowatt power levels of light to be used. This is not only a distinct improvement over the resulting current seen in this work, but an immense improvement over the earlier works depending on the relatively minor non-linearities (about five orders of magnitude less than metal-oxide-superconductor) of metal-oxide-metal elastic tunneling elements used in previous works.

At this point, one would have a high-speed electron tunneling element with a response time fast enough to permit the flow of optical current through the element at visible and UV frequencies. As a result of this, and again using the nonlinear current-voltage characteristics of the metal-oxide-superconductor tunneling element which permits it to be a broadband frequency mixer/multiplier, it is then capable of being used to directly mix the frequencies of lasers differing by several octaves -- the frequency of a microwave standard (or klystron) with that of an IR laser, the frequency of an IR laser with that of a visible laser, or even a UV laser -- thus eliminating the current multi-stage arrangement.

With the broadband frequency mixing capabilities, this extremely high-speed element makes it possible to construct a phase-locked frequency multiplier chain, forming a "transfer oscillator". It is this transfer oscillator that would consist of several phase-locked stages, thus extending the microwave frequency measurement technology well into the visible and even into the UV region. The immediate result of this extension will make it possible to measure the absolute frequencies of the visible and UV lasers used.

This has some severe, important, and beneficial implications for the science of spectroscopy, as well as for the time and length standards. In addition, it will now be possible to construct a master-clock oscillator

operating at an optical frequency with an output in the microwave region, the microwave output being phase-locked to the master optical clock. Or, conversely, it will be possible to construct a Cesium clock with an output at an optical frequency, with this optical output phase-locked to the Cesium clock frequency.

Throughout the above discussion regarding the future development of a true master-oscillator, and hence an optical clock, it must be realized that what is required is a laser with a highly reproducible and stable frequency. What makes it possible to have such a stable laser is the ability to "time" optical frequencies. This work demonstrates that the metal-oxide-superconductor electron tunneling element provides this ability once the impinging E-field is coupled across the barrier, resulting in the Fermi level being modulated at the applied optical frequency.

Appendices

Appendix 1 -- Justification of Matrix Element Remaining Unchanged when the Metal Goes Superconducting¹¹

An expression for the normal to superconducting current, I_{NS} , starting from microscopic theory was first given by Cohen *et al.* [37], and shortly thereafter Schrieffer [38-39] took a slightly modified approach. This explanation follows the latter article, after presenting some background information.

In 1957, Bardeen, Schrieffer and Cooper [40] offered the first microscopic theory of superconductivity. The main assumptions that are critical to this discussion were:

(a) The superconducting ground state can be expressed solely in terms of Cooper pairs so that the states $(\mathbf{k}, -\mathbf{k})$ are occupied or empty simultaneously (assuming that the spins are and remain antiparallel so as to have no need for spin indices).

(b) The various interactions may be taken identical in the normal and superconducting states and only the phonon and screened Coulomb interactions need to be separated for attention.

(c) The difference between the phonon and screened Coulomb interactions is $-V_{\mathbf{k}\mathbf{k}'}$ which may be expressed in the simple form

$$V_{\mathbf{k}\mathbf{k}'} = \begin{cases} V, & \text{for } |\epsilon_{\mathbf{k}}|, |\epsilon_{\mathbf{k}'}| \leq k\theta_D \\ 0, & \text{otherwise} \end{cases} \quad (\text{A1.1})$$

¹¹Background information taken from Ref[3].

where the energy ϵ_k is measured from the Fermi surface and θ_D is the Debye temperature. Now, admittedly, this is an obvious oversimplification which completely disregards the details of the interactions. On a basic level, though, it gives a good approximation because the superconducting properties (in reduced coordinates) are hardly dependent on crystal structure and normal state properties.

Therefore, in accordance with the above assumptions, the ground state energy of the superconducting state at $T = 0^\circ\text{K}$ (relative to the energy of the normal state) may be written as

$$W_S = 2 \sum \epsilon_k V_k^2 - V \sum u_k v_k u_{-k} v_{-k} \quad (\text{A1.2})$$

where v_k^2 is the probability of state $(\mathbf{k}, -\mathbf{k})$ being coupled and u_k^2 is the probability that it is empty. Obviously, then,

$$v_k^2 + u_k^2 = 1 \quad (\text{A1.3})$$

Now, the first term in (A1.2) gives the difference in kinetic energy between the superconducting and normal phases at $T = 0^\circ\text{K}$. The problem mathematically is to minimize the ground state energy as expressed in (A1.2) with respect to the probability v_k . This ends up being

$$v_k = \left[\frac{1}{2} \left(1 - \frac{\epsilon_k}{E_k} \right) \right]^{1/2} \quad (\text{A1.4})$$

where

$$E_k = \left[\epsilon_k^2 + \Delta_k^2 \right]^{1/2} \quad (\text{A1.5})$$

and Δ_k may be determined from an integral expression.¹²

Now, Schrieffer writes the matrix element in the form

$$|M_k|^2 = |T_k|^2 u_k^2 \quad (\text{A1.6})$$

Thus, the matrix element is not precisely identical to that in the normal state, since there is this additional factor of u_k^2 . In addition, another important difference is that there are two quasiparticle states for a value of energy above the gap as shown in Figure A1. Thus an electron of momentum k_l on the left side may tunnel both into k_{r1} and k_{r2} .

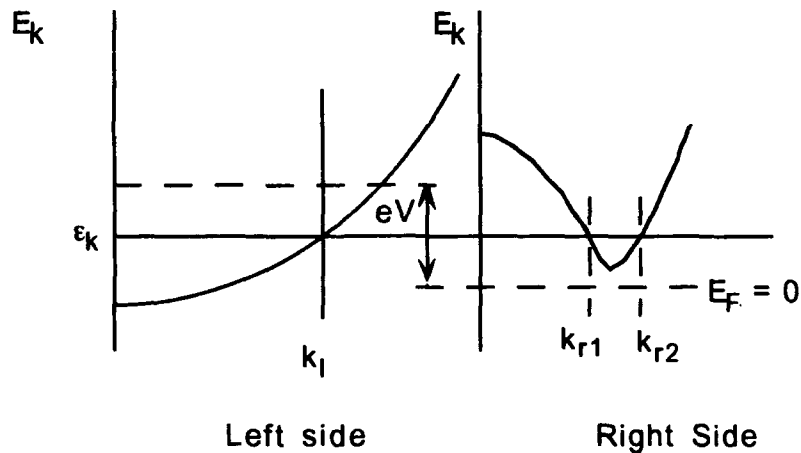


Figure A1 -- Energy-Momentum Diagram of an M-B-S Junction at an Applied Voltage, V , in the Schrieffer Quasiparticle Representation

¹²Interestingly, if we further assume

$$\Delta_k = \begin{cases} \Delta = \text{constant}, & \text{for } |\epsilon_k| < k\theta_D \\ 0, & \text{for } |\epsilon_k| > k\theta_D \end{cases}$$

and $\Delta \ll k\theta_D$, $N_N(\epsilon_k) \approx N_N(0)$ (where $N_N(0)$ is the density of states at the Fermi surface in the normal state), then a nicely simple expression may be obtained for the ground state energy

$$W_S = -\frac{1}{2} N_N(0) \Delta^2$$

Hence the current will be proportional to the sum

$$|T_H|^2 (u_{k_1}^2 + u_{k_2}^2) = |T_H|^2 \frac{1}{2} \left(2 + \frac{\varepsilon_{k_1}}{E_k} + \frac{\varepsilon_{k_2}}{E_k} \right) \quad (\text{A1.7})$$

But according to (A1.5) $\varepsilon_{k_1} = -\varepsilon_{k_2}$ and, hence, the result that the current is proportional to $|T_H|^2$. This, then, is the reason for the correctness of the simple tunneling picture and the phenomenological theory discussed in chapter 2.3.

Appendix 2 -- Faithful Four Pole Impedance Measurements

The technique used in this research to determine the impedance of the individual leads, as well as the impedance of the junctions was via "4-pole" measurements. The advantage here is that the lead resistances of the measuring circuit can be eliminated, thus, providing faithful readings of the object being measured.

"4-pole" measurements are conceptually depicted in Figure A2.1. Across two separate leads, a current (provided by the Bias Box current source) is introduced across the junction. From the juxtaposing quadrant, voltage measurements of the diode are then taken. It is this geometry of the circuit, combined with a large input impedance of the amplifiers that permit the faithful measurements.

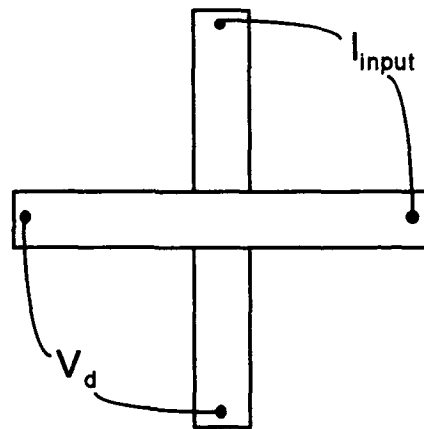


Figure A2.1 -- "4-Pole" Measurements of Junction Impedances

In Figure A2.2, a simplified circuit diagram represents the experimental arrangement, to include the voltage measurement loop. R_B is the bias resistor

in the Bias Box. The various R_L identified resistors represent the inherent impedance of the lines going to and coming from the junction. R_d is the representative impedance of the junction, and R_{amp} represents the input impedance of the opamp in the Amplifier Box.

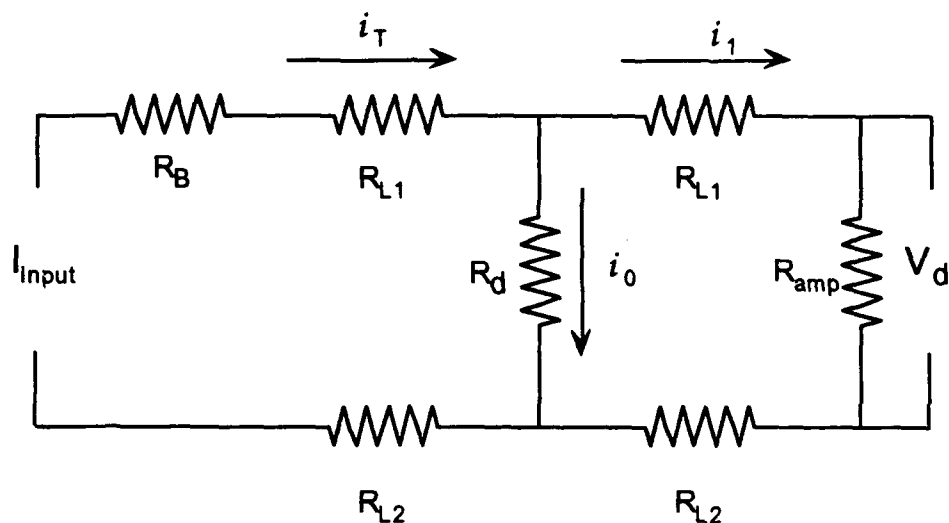


Figure A2.2 -- Circuit diagram for "4-Pole" Impedance Measurements

Obviously from Kirchoff's Current Law $i_T = i_1 + i_o$. In addition, following a standard approach for a current divider, it is possible to write

$$i_o = \frac{R_{L1} + R_{L2} + R_A}{(R_d + R_{L2}) + (R_{L1} + R_A + R_{L2})} i_T \quad (A2.1)$$

Now, rearranging a bit, gives

$$i_o = \frac{R_{L1} + R_{L2} + R_A}{(R_{L1} + R_{L2} + R_A) \left[1 + \frac{R_d + R_{L2}}{(R_{L1} + R_{L2} + R_A)} \right]} i_T \quad (A2.2)$$

In this form it is readily apparent what happens, since the fraction in the square brackets is denominated by R_A (which is on the order of 10^8 , and typically 5 orders of magnitude greater than R_d). Consequently,

$$\begin{aligned} i_o &= \frac{R_{L1} + R_{L2} + R_A}{(R_{L1} + R_{L2} + R_A)} i_T \\ &= i_T \end{aligned} \tag{A2.3}$$

This indicates that all of the original current, i_T , flows through the diode, thus allowing faithful voltage and, therefore, impedance measurements across it.

Appendix 3 -- Numerical Integration Using the MIT Cray X-MP Supercomputer

In order to calculate the I-V and I''-V responses, it was necessary to perform numerical integrations on the integral in equation (2.3.5) and its associated derivatives. After applying two coordinate transformations, equation 2.3.5 loses its integratable singularity, and is placed into a computer convenient form. Beginning with the basic form of the above integral,

$$I_{NS} = A N_{IN}(0) N_{rN}(0) \int \frac{|E| [f(E-eV) - f(E)] dE}{(E^2 - \Delta^2)^{1/2}} \quad (A3.1)$$

Integrating for all possible energies yields

$$I_{NS} = \int_{\Delta}^{\infty} \frac{E [f(E-eV) - f(E)] dE}{(E^2 - \Delta^2)^{1/2}} - \int_{-\Delta}^{-\infty} \frac{E [f(E-eV) - f(E)] dE}{(E^2 - \Delta^2)^{1/2}} \quad (A3.2)$$

Introducing $x + \Delta = E$ in the first integral and $x + \Delta = -E$ in the second transforms (A3.2) into

$$I_{NS} = \int_0^{\infty} \frac{(x + \Delta) [f(x + \Delta - eV) - f(x + \Delta)] dx}{[x(x + 2\Delta)]^{1/2}} + \int_0^{\infty} \frac{(x + \Delta) [f(-x - \Delta - eV) - f(-x - \Delta)] dx}{[x(x + 2\Delta)]^{1/2}} \quad (\text{A3.3})$$

Now using the general relationship valid for the Fermi function

$$f(-\xi) = 1 - f(\xi) \quad (\text{A3.4})$$

and carrying out the algebra gives

$$I_{NS} = \int_0^{\infty} \frac{(x + \Delta) [f(x + \Delta - eV) - f(x + \Delta + eV)] dx}{[x(x + 2\Delta)]^{1/2}} \quad (\text{A3.5})$$

This hasn't quite removed the singularity but allowing the substitution of $u^2 = x$ will. Rewriting (A3.5) with this substitution and then simply changing the dummy variable back to x yields

$$I_{NS} = \int_0^{\infty} \frac{2(x^2 + \Delta) [f(x + \Delta - eV) - f(x + \Delta + eV)] dx}{[x^2 + 2\Delta]^{1/2}} \quad (\text{A3.6})$$

Finally, this integrand is in a convenient form with which to complete the numerical integrations. It is with (A3.6) that the included FORTRAN program executed, to include the accompanying derivatives.

The D01AHE - NAG FORTRAN library routine computes a definite integral of the form $\int_A^B f(x) dx$. The method uses as its basis a family of interlacing

high precision rules as outlined in reference [41]. Two advantages of this specific subroutine include:

(a) The rate of convergence is monitored and used to make a decision to abort and subdivide before the full sequence has been applied.

(b) The relative accuracy sought in each subinterval is adjusted in accordance with its likely contribution to the total integral.

The subroutine parameters and call are as follows:

```
real FUNCTION D01AHE (A,B,EPSR,NPTS,RELERR,F,NLIMIT,IFAIL)
INTEGER NPTS, NLIMIT, IFAIL
REAL A,B,EPSR,RELERR,F
EXTERNAL F
```

where,

A -- lower bound of integral

B -- upper bound

EPSR -- specifies relative accuracy required

NPTS -- counter for the number of evaluations used

RELERR contains the relative error achieved (rough guess)

F -- is the function supplied by the user

NLIMIT -- specifies the limit of the number of function evaluations;
default is 10,000

IFAIL -- is a flagged fail message

```

      Program FIT5
C
C This version computes I(V), d1iv, d2iv,d1iT (correctly!) all with
C delta a function of temperature. The d2iT calculations have been
C removed. Tc is assigned inside the program, not as an interactive
C input. In addition, this computes d3idv3.
C
      Common/TJ/ delta, T, v, beta, SQTgap, Tc
      Real D2iVo(1000), Volts(1000), Predi(1000)
      Real D1iVo(1000), D1iTe(1000), D3iVo(1000)
      Real Cerror(1000), Verror(1000)
      Real vstep, vrangel, vrange2, EPSR, RELERR, high
      Real D01AHE
      Integer IFAIL, NLIMIT, I
      External current, d2iv, d1iv, d1iT, d3idv3
C
C
C
      NLIMIT = 0
      EPSR = 1.0E-6
      IFAIL = 0
C
C2345678
C
      Write(*,*) 'Input T (should NOT be higher than Tc = 6.79768): '
      Read(*,10) T
10      Format(F10.4)
      Write(*,*) 'Input Vstep size: '
      Read(*,10) vstep
      Write(*,*) 'Beginning Voltage(mV): '
      Read(*,10) vrangel
      Write(*,*) 'Ending voltage(mV): '
      Read(*,10) vrange2
C
C2345678
C
      high = (vrange2 - vrangel) / vstep
      beta = 1./(.086 * T)
      Tc = 6.79768
      SQTgap = SQRT(1 - (T/Tc) )
      delta = 1.6 * 0.086 * Tc * SQTgap
C
C
C
      Open(unit = 16, file = 'curves.out', form = 'formatted',
$       status = 'new')
C       Open(unit = 17, file = 'errors.out', form = 'formatted',
$       status = 'new')
C
C
C
      Write(*,20) T, delta, vstep

```

```

Write(16,20) T, delta, vstep
C   Write(17,20) T, delta, vstep
20  Format('Temperature= ',F10.4/,'Delta= ',F10.4/,'Volt Step= ',
$                                     F10.4//)
Write(16,30)
30  Format('Volts(mV)',1X,'Current',1X,'2d-Deriv(V)',1X,
$      '1st-Deriv(V)',1X,'1st-Deriv(T)',1X,'3rd-Deriv(V)')
C
C
C
C
DO 35 I = 1, high+1
v = (I-1) * vstep + vrangel
Volts(I) = v
Predi(I) = D01AHE(0.,vrange2 + 3,EPSR,NPTS,RELERR,
$   current,NLIMIT,IFAIL)
Cerror(I) = RELERR
D2iVo(I) = D01AHE(0.,vrange2+3.,EPSR,NPTS,RELERR,
$   d2iv, NLIMIT,IFAIL)
Verror(I) = RELERR
D1iVo(I) = D01AHE(0.,vrange2+3.,EPSR,NPTS,RELERR,
$   d1iv,NLIMIT,IFAIL)
D1iTe(I) = D01AHE(0.,vrange2+3.,EPSR,NPTS,RELERR,
$   d1iT,NLIMIT,IFAIL)
D3iVo(I) = D01AHE(0.,vrange2+3.,EPSR,NPTS,RELERR,
$   d3idv3,NLIMIT,IFAIL)
35  CONTINUE
C
C
C2345678
Write(16,40) (Volts(I), Predi(I), D2iVo(I),
$   D1iVo(I), D1iTe(I),D3iVo(I), I = 1, high+1)
40  Format(E13.7, 1X, E13.7, 1X, E13.7, 1X, E13.7,1X,E13.7,
$      1x,E13.7)
C
C
C
C   Write(17,50)
C50  Format('Volts(mV)',1X,'(C)error',1X,'(V)error')
C   Write(17,40) (Volts(I),Cerror(I), Verror(I),
C   $           I = 1, high + 1)
C
C
C   Close (unit = 16, status = 'keep')
C   Close (unit = 17, status = 'keep')
C
C
C   End
C
C
C2345678
Real Function current(x)
Common/TJ/ delta, T, v, beta, SQTgap, Tc
Real x,g1,g2,sn

```

```

g1 = exp (beta * ((x**2) + delta - v) )
g2 = exp (beta * ((x**2) + delta + v) )
sn = ((x**2) + delta) / SQRT((x**2) + 2*delta)
current = 2 * sn * ( (1/(1 + g1) ) - 1 / (1 + g2) )
Return
End

```

C
C
C
C

```

Real Function d2iv(x)
Common/TJ/ delta, T, v, beta, SQTgap, Tc
Real v,delta,x,g1,g2,g3,g4,sn
g1 = exp (beta * ((x**2) + delta - v) )
g2 = exp (beta * ((x**2) + delta + v) )
sn = ((x**2) + delta) / SQRT((x**2) + 2*delta)
g3 = g1 * (g1-1) / (1 + g1)**3
g4 = g2 * (g2-1) / (1 + g2)**3
d2iv = 2 * sn * (beta**2) * (g3 - g4)
Return
End

```

C
C
C

```

Real Function dliv(x)
Common/TJ/ delta, T, v, beta, SQTgap, Tc
Real T, v, delta,x,g1,g2,sn
g1 = exp (beta * ((x**2) + delta - v) )
g2 = exp (beta * ((x**2) + delta + v) )
sn = ((x**2) + delta) / SQRT((x**2) + 2*delta)
dliv = 2*sn*beta* ((g1/(1+g1)**2) + g2/(1+g2)**2)
Return
End

```

C
C2345678
C

```

Real Function dliT(x)
Common/TJ/ delta, T, v, beta, SQTgap, Tc
Real T, v, delta,x,g1,g2,sn
g1 = exp (beta * ((x**2) + delta - v) )
g2 = exp (beta * ((x**2) + delta + v) )
sn = ((x**2) + delta) / SQRT((x**2) + 2*delta)

```

C
C The following gobbledegook is the 1st derivative of current w.r.t
C temperature.

C
C2345678

```

dliT = -0.1376*(1/(1 + g1) - 1/(1 + g2))/
$ (SQTgap*Sqrt(0.2752*SQTgap*Tc + x**2)) +
$ 0.1376*(1/(1 + g1) - 1/(1 + g2))*(x**2 + delta)/
$ (SQTgap*(0.2752*SQTgap*Tc+ x**2)**(3/2)) +
$ 2*sn*(-(g1*(-0.8/(T*SQTgap) -
$ 11.6279*(-v + x**2 + delta)/T**2)/(1 + g1)**2)
$ + g2*(-0.8/(T*SQTgap) -

```

```

$          11.6279*(v + x**2 + delta)/T**2)/(1 + g2)**2)
Return
End

C
C2345678
C
Real Function d3idv3(x)
Common/TJ/ delta, T, v, beta, SQTgap, Tc
Real T, v, delta,x,sub1,sub2,TK3,sn
sub1 = exp((1.6*0.086*SQTgap*Tc + v + x**2) / (.086*T))
sub2 = exp((1.6*0.086*SQTgap*Tc - v + x**2) / (.086*T))
sn = ((x**2) + delta) / SQRT((x**2) + 2*delta)
TK3 = (0.086*T)**3

C
C The following gobbledegook is the 3rd derivative of current w.r.t
C voltage.
C
C23456789
d3idv3 = 2*sn*((6*sub1**3)/((1 + sub1)**4*TK3) -
$ 6*sub1**2/((1 + sub1)**3*TK3) +
$ sub1/((1 + sub1)**2*TK3) +
$ (6*sub2**3)/((1 + sub2)**4*TK3) -
$ 6*(sub2**2)/((1 + sub2)**3*TK3) +
$ sub2/((1 + sub2)**2*TK3))
Return
End

```

References

- 1 G.M. Elchinger, "Properties of Metal-Barrier-Metal Tunneling Junctions Responding to Infrared and Visible Radiations", (PhD. thesis, Mass. Inst. of Tech., 1978)
- 2 K.C. Liu, "Characteristics of Point Contact Submicron Junctions and Their Applications", (PhD. thesis, Mass. Inst. of Tech., 1979)
- 3 L. Solymar, *Superconductive Tunnelling and Applications*, (Wiley-Interscience, New York, 1972)
- 4 L.O. Hocker, and A. Javan, "Laser Harmonic Frequency Mixing of Two Different Far Infrared Laser Lines up to 118 μ m", *Phys. Lett.* **26A**, 255-6 (1968)
- 5 L.O. Hocker, D.R. Sokoloff, V. Daneu, A. Szoke, and A. Javan, "Frequency Mixing in the Infrared and Far-Infrared Using a Metal-to-Metal Point Contact Diode", *App. Phys. Lett.* **12**, 401-2 (1968)
- 6 M. Heiblum, S.Y. Wang, J.R. Whinnery, and T.K. Gustafson, "Characteristics of Integrated MOM Junctions From DC to Optical Frequencies", *J. Quantum Elect.* **13**, 48 (1977)
- 7 J.G. Small, G.M. Elchinger, A. Javan, A. Sanchez, F.J. Bachner, and D.L. Smythe, "AC Electron Tunneling at Infrared Frequencies: Thin Film M-O-M diode Structures With Broad-Band Characteristics", *App. Phys. Lett.* **24**, 275 (1974)
- 8 T.K. Gustafson, R.V. Schmidt, and J.R. Perucca, "Optical Detection in Thin Film Metal-Oxide-Metal Diodes", *App. Phys. Lett.* **24**, 620 (1974)
- 9 S.Y. Wang, T. Izawa, and T.K. Gustafson, "Coupling Characteristics of Thin-Film Metal-Oxide-Metal Diodes at 10.6 μ m", *App. Phys. Lett.* **27**, 481 (1975)
- 10 B. Fan, S.M. Farris, T.K. Gustafson, and T.J. Bridges, "Nonlinear Optical Response of Metal-Barrier-Metal Junctions", *App. Phys. Lett.* **30**, 177 (1977)

- 11 Richard L. Liboff, *Introductory Quantum Mechanics*, (Addison-Wesley Publishing Company, New York, 1989)
- 12 Claude Cohen-Tanoudji, Bernard Diu, and Franck Laloë, *Quantum Mechanics*, (John Wiley and sons, New York, 1977)
- 13 J.G. Simmons, "Generalized Formula for the Electric Tunnel Effect Between Similar Electrodes Separated by a Thin Insulating Film", *J. App. Phys.* **34**, 1793-1803 (1963)
- 14 R. Stratton, "Volt-Current Characteristics for Tunneling Through Insulating Films", *J. Phys. Chem. Solids* **23**, 1177-1190, (1962)
- 15 E.O. Kane, "Basic Concepts of Tunneling", *Tunneling Phenomena in Solids*, E. Burstein and S. Lundquist, eds., (Plenum Press, New York, 1969)
- 16 J. Bardeen, *Phys. Rev. Letts.* **6**, 57-9 (1961)
- 17 I. Giaever, "Energy Gap in Superconductors Measured by Electron Tunneling", *Phys. Rev. Lett.* **5**, 147-8 (1960)
- 18 J.C. Fischer and I. Giaever, "Tunneling Through Thin Insulating Layers", *J. App. Phys.* **32**, 172-177 (1961)
- 19 I. Giaever and K. Megerle, "Study of Superconductors by Electron Tunneling", *Phys. Rev. Letts.* **14**, 108 (1965)
- 20 A. Dayem and R.J. Martin, "Quantum Interaction of Microwave Radiation with Tunneling Between Superconductors", *Phys. Rev. Letts.* **8**, 246 (1962)
- 21 P.K. Tien and J. Gordon, "Multiphoton Process Observed in the Interaction of Microwave Fields with the Tunneling Between Superconductor Films", *Phys. Rev.* **129**, 647 (1963)
- 22 Y. Goldstein and B. Abeles, "Superconducting Tunneling Induced by Gigacycle Sound Waves", *Phys. Letts.* **14**, 78 (1965)
- 23 E. Lax and F.L. Vernon, Jr., "Microwave Phono-Assisted Tunneling in Superconductors", *Phys. Rev. Letts.* **14**, 256 (1965)
- 24 B.N. Taylor and E. Burstein, "Excess Currents in Electron Tunneling Between Superconductors", *Phys. Rev. Letts.* **10**, 14 (1963)

- 25 C.J. Adkins, "Two particle Tunneling Between Superconductors", *Phil. Mag.* **8**, 1051 (1963)
- 26 J.M. Rowell, "Tunneling Between Superconductors", *Rev. Mod. Phys.* **36**, 215 (1964)
- 27 I.K. Yanson, V.M. Svistunov and I.M. Dmitrenko, "Experimental Observations of Tunneling of Cooper Pairs Between Thin Layers of Superconducting Tin", *JETP* **20**, 1404 (1965)
- 28 W.J. Tomasch, "Geometrical Resonance in the Tunneling Characteristics of Superconducting Pb", *Phys. Rev. Letts.* **15**, 672 (1965)
- 29 Z. Burshtein and J. Levinson, "Photo-induced Tunnel Currents in Al-Al₂O₃-Au Structures", *Phys. Rev. B* **12**, 3453-7 (1975)
- 30 R.C. Jaklevic and J. Lambe, "Molecular Vibration Spectra By Electron Tunneling", *Phys. Rev. Lett.* **17**, 1139-40 (1966)
- 31 A. Braunstein, M. Braunstein, and G.S. Picus, "Photoemissive Determination of Barrier Shape in Tunnel Junctions", *Phys. Rev. Lett.* **14**, 219-21 (1965)
- 32 G.M. Elchinger, A. Sanchez, C.F. Davis, and A. Javan, "Mechanism of Detection of Radiation in a High-Speed Metal-Metal Oxide-Junction in the Visible Region and at Longer Wavelengths", *J. App. Phys.* **47**, 591-4 (1976)
- 33 A. Sanchez, C.F. Davis, G. Lui, and A. Javan, "The MOM Tunneling Diode; Theoretical Estimate of its Performance at Microwave and Infrared Frequencies," *J. Appl Phys.* **49**, 10 (1978)
- 34 J. Vrba, and S.B. Woods, "Glow-Discharge of Freshly Evaporated Aluminum Films", *Can. J. Phys.* **50**, 548-52 (1972)
- 35 J.L. Miles, and P.H. Smith, "The Formation of Metal Oxide Films Using Gaseous and Solid Electrolytes", *J. Electrochem. Soc.* **110**, 1240-5 (1963)
- 36 D.E. Thomas and J.M. Rowell, "Low Level Second Harmonic Detection System," *Rev. Sci. Instr.* **36**, 9 (1965)
- 37 M.H. Cohen, L.M. Falicov and J.C. Phillips, "Superconductive Tunneling", *Phys. Rev. Letts.* **8**, 316 (1962)

- 38 J.R. Schrieffer, " Single Particle Tunneling in Superconductors", *Tunneling Phenomena in Solids*, E. Burstein and S. Lundquist, eds., (Plenum Press, New York, 1969)
- 39 J.R. Schrieffer, "Theory of Electron Tunneling" *Rev. Mod. Phys.* **36**, 200 (1964)
- 40 J. Bardeen, L.N. Cooper, and J.R. Schrieffer, "Theory of Superconductivity", *Phys. Rev.* **108**, 5, 1175-1204 (1957)
- 41 T.N.L. Patterson, "The Optimum Addition of Points to Quadrature Formulae", *Math. Comp.* **22**, 847-856 (1968)
- 42 K.W. Sheppard, "Photocurrents Through Thin Films of Al_2O_3 " *J. App. Phys.* **36**, 796 (1965)
- 43 J.D. Jackson, *Classical Electrodynamics*, (John Wiley and Sons, New York, 1975)
- 44 V.E. Grüneisen, "Die Abhängigkeit des elektrischen Widerstandes reiner Metalle von der Temperatur", *Ann. d. Phys.* **5**, 16, 530-540 (1933)
- 45 H.A. Boorse, and H. Niewodniczanski, "The Electrical Resistance of Aluminum at Low Temperatures", *Proc. Roy. Soc. A* **153**, 463 (1936)
- 46 J.G. Thomas and E. Mendoza, "LXXXVI. The Electrical Resistance of Magnesium, Aluminum, Molybdenum, Cobalt, and Tungsten at Low Temperatures", *Phil. Mag.*, 900-910 (1951)
- 47 D. Chaverri, A. Saenz, and V. Castano, "Grain Size and Electrical Resistivity Measurements on Aluminum Polycrystalline Thin Films", *Materials Letters* **12**, 344-348 (1991)
- 48 K.M. Evenson, D.A. Jennings, F.R. Peterson, and J.S. Wells, *Laser Spectroscopy III*, J.L. Hall and L.L. Carlsten, eds., (Springer-Verlag, Berlin, 1977), pp 56-68.
- 49 L.O. Hocker, J.G. Small, and A. Javan, "Extension of Absolute Frequency Measurements to the 84μ Range", *Phys. Letts.* **29A**, 6, 321-2 (1969)
- 50 E.N Economou, "Surface Plasmons in Thin Films", *Phys. Rev.* **182**, 2, 539 (1969)